Int J Adv Manuf Technol (2017) 92:2881–2918
DOI 10.1007/s00170-017-0334-x

ORIGINAL ARTICLE

VFCVD diamond-coated cutting tools for micro-machining titanium alloy Ti6Al4V

Mark J. Jackson [1,2] · **Tamara Novakov** [1] · **Michael Whitfield** [1] · **Grant Robinson** [1] · **Rodney Handy** [1] · **Htet Sein** [3] · **Waqar Ahmed** [4]

Received: 29 December 2016 / Accepted: 22 March 2017 / Published online: 12 April 2017
© Springer-Verlag London 2017

Abstract Diamond-coated cutting tools are known to machine complex materials with many benefits associated with the generation of lower temperatures between contact surfaces. However, the complexity associated with machining exotic materials at the micro-scale eludes many researchers who study phenomena pertinent to the development of new processes for novel micro-structured materials. The study investigated the use of a Lagrangian-Eulerian-formulated finite element program to analyze chip formation and thermal effects when micro-machining Ti6Al4V titanium alloy used for medical device applications. For the simulated machining conditions described in this paper, chip formation occurred when $F_C/F_T > 1$ and burr formation occurred when $F_C/F_T < 1$. In addition to the force conditions, when the ratio of feed per tooth to tool edge radius is approximately unity ($f_{tooth}/t_r \sim 1$), the micro-machining process forms chips. When the ratio is decreased to equal 0.5 ($f_{tooth}/t_r = 0.5$), chip formation and burr formation exists simultaneously. However, when the ratio approaches an approximate value of 0.3 ($f_{tooth}/t_r \sim 0.3$), burr formation is dominant. The study also provides an insight into the thermal effects of micro-machining that shows how vertical filament chemical vapor deposition (VFCVD)-coated tools maintain the integrity of the surfaces of the material as a function of simulated machining parameters. In conclusion, the computational analysis is compared with practical micro-machining results reported in the literature.

Keywords Diamond tools · Finite elements · Titanium alloy · Micro-machining

1 Introduction

Traditionally, micro-machining includes "bulk" micro-machining processes that produce features inside a substrate material, while "surface" micro-machining processes are produced by deposition and etching of different structural layers on top of the substrate. In "mechanical" micro-machining, the material removal process resembles macroscopic machining processes such as drilling, milling, and turning. Micro-machining encompasses micro-electro-mechanical systems (MEMS), nanoelectro-mechanical systems (NEMS), micro-systems technologies (MST), and processes related to the production and packaging of micro-systems. Micro-machining by precision processes such as three- dimensional micro-electro-discharge machining (μ-EDM), micro-laser machining, micro-cutting, and micro-grinding, can produce microscopic and mesoscopic mechanical structures of complexity and in engineering materials (other than silicon). Compared with precision machining, micro-machining aims to produce feature sizes that are typically 1 to 100 μm in size with sufficient tolerances to achieve the required functionality and repeatability. The range of machining accuracy between 0.01 μm (lower range of precision machining) and 0.001 μm (1 nm) is termed as ultra-precision machining. Figure 1 shows the capability of conventional micro-machining in relation to other manufacturing processes such as laser machining, EDM, grinding and the LiGA (photo-lithography method using synchrotron radiation) process [1]. It

✉ Mark J. Jackson
jacksonmj04@yahoo.com

[1] Center for Advanced Manufacturing, Purdue University, West Lafayette, IN, USA

[2] Kansas State University, Manhattan, KS, USA

[3] Department of Chemistry, Manchester Metropolitan University, Manchester, UK

[4] School of Mathematics and Physics, University of Lincoln, Lincoln, UK

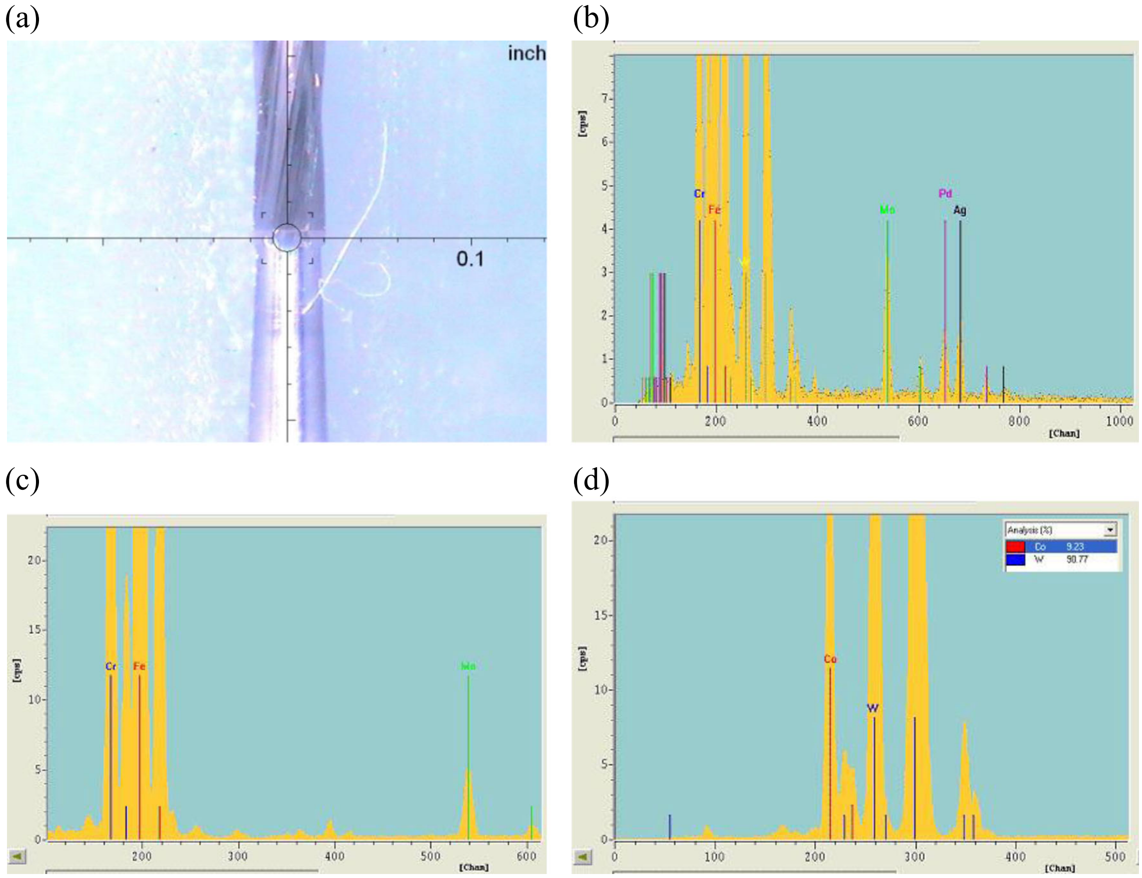

Fig. 1 Diamond-coated micro-cutting tool prior to diamond deposition showing: **a** cross-section of the tool showing cutting head, brazed section, and shank; **b** EDX spectrum of brazed section showing iron and chromium; **c** EDX spectrum of shank showing iron and chromium elements; and **d** EDX spectrum of the cutting section of the tool showing cobalt (Co ~9.23 wt.%) and tungsten (W ~90.77 wt.%)

is worth noting that micro-machining generates surface roughness (Ra) values to the nanometer range (to almost 5 nm for feature sizes to 1 μm). In contrast, for "normal machining processes," surface roughness values from 10 to 100 μm can be achieved. Currently, the following areas of industry are showing interest in micro-machining:

i. Medical and electronic industries are the most active in this area, and in both cases, the goals are the same, which is making smaller parts with more capabilities;
ii. Medical industry is under pressure to produce various repair and pain-relief devices, which must be small enough to embed into the human body. Micro-sized components can lead to the progression of minimally invasive techniques for orthopedic, cardiologic, and neurologic applications;
iii. Aerospace industry is a large end user for fasteners, fittings, sensors, and various flow-control devices; and
iv. Automotive industry. Many automotive features require very small motors and actuators. From a construction point of view, there is a trend to install complex micro-scale fuel injection and flow-control elements. Some of the most representative examples in this category are micro-valves and fluidic graphite channels (circuits) for fuel cell applications.

Companies involved in micro-manufacturing originally came from three sources. First, a number of companies have been successful in the micro-market for some time, such as those involved with micro-turning using Swiss lathes. The second source consisted of manufacturers who have modified their equipment to meet the special needs of micro-manufacturing. For example, many tool builders have generated lines of small tools for use on macro-machine tools. The third source was created by entrepreneurs who, in the last few years, introduced totally new products for the micro-market such as desktop machine tools and robots. Of these three sources, micro-milling has been developing rapidly to meet demand [2].

Mechanical micro-milling is not generally applied for micro-machining due to substantial difficulties in obtaining the appropriate micro-tools. The comparison between capabilities of the micro-milling process and other non-mechanical micro-machining processes is given in Table 1.

Table 1 Listing of micro-machining techniques and their capabilities in comparison with standard high-speed milling (HSM)

Micro-machining capabilities

	High-speed milling	Sinker EDM	Wire EDM	X-ray lithography	Ion beam machining
Minimum structure size (μm)	50	5 to 10	15–20	–	<0.1
Surface finish Ra (μm)	1	0.2	0.05	–	0.04 to 0.15
Radius (μm)	50	<10	~15	–	0.01
Aspect ratio	100–150	~20	100–150	100	10
Disadvantage	Thermal fracture	Slow removal rates	Through-features only	Learning curve for moldmakers	Learning curve for moldmakers

However, precision micro-milling has various features depending on the tool shape and the kinematics. The most complex is three-dimensional micro-milling of cavities in miniaturized molds, chemical micro-reactors, and micro-fluidic parts. Fly milling is basically a method for producing grooves when they are cut in different directions. It is particularly effective for producing a large number of micro-column arrays. Single crystal diamond with a cutting edge radius of 50 nm is the preferred tool material and geometry for conventional micro-cutting of non-ferrous materials such as brass, aluminum, copper, and electroless nickel. This method allows one to produce V-shaped grooves with high form accuracy without burrs and a surface roughness, Rz ~48 nm. Another example of the application for micro-diamond machining are the machining of flow passages for micro-compact heat exchangers, in which surface enhancement is necessary to reduce boundary convection resistances. The machined channels are 100 μm in width and 80 μm in depth (The material used is usually high conductivity copper foil of 125 μm thickness). Micro-diamond machining can also be used to complement the lithography process. Tungsten carbide tools with extremely small cutting edge radii can produce surface roughness values lower than Rz ~0.8 μm when micro-milling steel miniatures [3].

The size of precision micro-cutting tools determines the limit of the size and accuracy of micro-structured features. Diamond tools are often used for ultra-precision machining but are limited to machining non-ferrous materials. Therefore, micro-tools such as micro-end mills and drills are generally made from tungsten carbide bonded with cobalt with grain sizes smaller than 600 nm. Micro-milling tools can have a number of different, but simple cross-sectional profiles. The first two profiles are used in D-shape and spade micro-drills in which the cutting part is much shorter in length. In addition, they have a flat front plane and the clearance angle on the major cutting edges equals 0°. Some cross-sections have regular polygonal forms and large negative rake angle, usually between −45° and −60°. The side surfaces in micro-drills can be shaped as concave surfaces which improve cutting performance. It is reported that besides using micro-end mills, slotting micro-mills with the minimum width of about 50 μm are widely used in the micro-machining industry. Tools with a diameter of 2 mm and a width of 30 μm are fabricated from diamond-like carbon (DLC) layers using the CVD technique. Milling tools capable of generating features that are 25 μm in size are made by sculpting carbide and HSS blanks using a focused ion beam. End mills made in this way can be as small as 20 μm in diameter and turning tools can be roughly 10 μm in width. These types of tools are used in the meso-machining of miniature nuclear weapon components made of aluminum, brass, and 4340 steel. When shaping tools with an ion beam, it is difficult to generate the fluted, complex geometry that is typical of a standard end mill. Instead, meso-machining end mills have simple geometric cross-sections where the cutting edges are obtained by intersecting two planes without a helix angle. A typical depth of cut is 1 μm when milling slots between 20 and 30 μm wide in the three materials selected. Commercially available tungsten carbide micro-end mills with helix flutes produced by grinding can be as small as 50 μm in diameter [4].

For micro-machining applications, diamond micro-cutting tools are typically tungsten carbide tools coated with a thin film of diamond. A modified hot filament chemical vapor deposition known as vertical filament chemical vapor deposition (VFCVD) system enables a micro-cutting tool substrate to be negatively biased with respect to the filament prior to diamond deposition. In the cases where the substrates are negatively biased, prior to substrate biasing, the filament is pre-carburized for 15 min under standard horizontal filament chemical vapor deposition (HFCVD) conditions using a 3% methane concentration to avoid tantalum contamination [5]. The HFCVD system can be divided into three main components: the gas supply system; HFCVD process chamber; and the pumping system. Firstly, the reactant gases, typically an excess of H_2, CH_4, and, if required, Ar, are delivered to a pre-mixing manifold via separate mass flow controllers before being admitted to the process chamber. This arrangement, allows the various hydrogen, methane, and argon rations to be set independently for a total flow-rate of 200 sccm. A water-cooled stainless steel reaction chamber houses a removable substrate-filament assembly located in the plane of a viewing glass window. Gas activation is achieved using a single 0.5 mm diameter tantalum filament of 100 mm total length, which is coiled and supported by stainless steel rods leading to an isolated power source made of copper rod. This ensures that maximum power dissipation is restricted to the filament section of the complete heating circuit. The filament is powered by a 2.5-kW DC power supply.

The substrate temperature is measured with an insulated type-K thermocouple embedded in a substrate holder parallel with the substrate. The substrate mounting and heating assembly could be translated with respect to the filament within 0.1 mm, allowing both accurate and reproducible sample positioning. Pumping is achieved via a single-stage rotary pump, which achieved a base pressure of 1×10^{-3} Torr measured using a Pirani gauge located at the back of the chamber. The total process pressure, typically of the order of 20 Torr (2.66 kPa) is measured using a Bourdon pressure gauge.

To optimize the VFCVD process to grow high-quality diamond films, the deposition conditions are carefully controlled. The parameters influencing gas activation are the type of filament material (before and after carburisation), filament temperature, and filament geometry, and also the filament-substrate distance. Since all these factors influence the concentration of activated species reaching the substrate surface, they must be optimized. The initial deposition experiments were carried out to characterize the VFCVD system and hence determining the optimum conditions for diamond synthesis had been established. Deposition conditions were modified along with the design and process parameters to obtain polycrystalline diamond films similar to those obtained in prior investigations [5].

In the HFCVD system, the mechanism of heat transfer is the driving force in the chamber. In addition to radiation, convection, and conduction, heat transfer is also achieved via atomic hydrogen since the formation of atomic hydrogen at, or near to, the filament surface is endothermic. Atomic hydrogen readily recombines on solid surfaces to form molecular hydrogen with the recombination reaction being exothermic. Thus, atomic hydrogen acts as a carrier of heat from the filament to the growth surface. Since the quality, morphology, and defect density of diamond films are sensitive to temperature, a uniform substrate temperature is critical for the deposition of diamond films with uniform properties. Therefore, the heat transfer to the substrate and the resulting substrate temperature distribution are important considerations in the design of reactors for coating large areas and the deposition of complex-shaped substrates [6].

1.1 Thin film deposition of micro-tools

Cobalt-cemented tungsten carbide (WC-Co) micro-tools, 30 mm in length including the cutting head (WC-Co), shaft (Fe/Cr), and brazed section that is ~1.00 mm in diameter, were used in this study. Prior to pre-treatment, the tools were ultrasonically cleaned in acetone for 10 min to remove any loose residues present. Adhesion strength to diamond films is relatively poor, and on cemented carbide surfaces can lead to catastrophic failure of the coating during metal cutting. The poor adhesion is related to the cobalt binder that is present to increase the toughness of the tool, but it suppresses diamond nucleation and causes deterioration of diamond film adhesion. The following chemical etching procedure was used to remove the cobalt from the tool's surface. The cutting tools were ultrasonically cleaned in acetone for 10 min in order to remove loose residues from the surface. The first etching step uses Murakami's reagent ((10 g $K_3Fe(CN)_6$) + 10 g KOH + 100 ml water) to etch the surface and was carried out for 10 min in an ultrasonic bath followed by a rinse with distilled water. The second step etching was performed using an acid solution of hydrogen peroxide (3 ml (96 wt.%) H_2SO_4 + 88 ml (30% *w*/*v*) (H_2O_2)) for 10 s to remove Co from the surface. The substrates were then washed again with distilled water in an ultrasonic bath.

When applying a negative bias to the substrate the nucleation density, adhesion, and surface properties of the resulting diamond film can be improved. The effects of various process parameters such as bias time, emission current, bias voltage, and the filament arrangement on the film properties have been thoroughly investigated. Nucleation of diamond is an important step in the growth of diamond thin films, because it strongly influences diamond growth, film quality, and morphology. Generally speaking, seeding or abrading with diamond powder or immersing in diamond paste containing small crystallites processed in an ultrasonic bath enhances nucleation. One of the most promising in situ methods for diamond nucleation enhancement is substrate biasing. In this method, the substrate is biased negative during the initial stage of deposition. Positive substrate biasing can also be applied but is less commonly used [7].

The plasma generated during deposition consists of a non-trivial atmosphere of positive and negative ions, radicals, and neutrals. Negatively biasing the substrates causes positive ions to be accelerated towards the substrate thus enhancing adhesion of the growing diamond film. In addition, biasing is a highly controlled and is a non-destructive way of creating nucleation sites for the growth of diamond, while ion bombardment moves atoms around the surface breaking clusters of nucleated diamonds into a regulated thin solid film.

Negative bias voltages of ~300 V are applied to substrates relative to the filament. This produces emission currents of 200 mA or less. The nucleation times are typically between 10 and 40 min, and the input gas mixture during bias-enhanced nucleation (BEN) is typically a 3% CH_4 gas in gaseous H_2 at a pressure of 20 Torr (26.6 kPa). In the BEN process, electrons are emitted from diamond-coated molybdenum substrate holders and accelerate towards the filament gaining energy from the surrounding electrical field. These energetic electrons enable the ionization of hydrocarbon process gas mixtures. When the negative bias is applied to the anode, the voltage is gradually increased until a stable emission current is established and a luminous purple-colored gas discharge, typical of hydrogen-rich atmospheres, is formed in close proximity to the substrate [8].

1.2 Controlling structure and morphology

Deposition of high-quality adherent diamond to substrates such as cemented carbide, stainless steel, and various metal alloys containing transition elements present a considerable challenge due to poor adhesion and low nucleation density. Feed gases such as methane and hydrogen are commonly used to grow diamond films of high quality. These films have been found to be rough and brittle. For smooth, hard, and tough films, a different solution is needed for a number of applications especially involving metal substrates where thin films tend to delaminate due to thermally induced residual stresses. For many applications, the films need to adhere strongly to the surface and have the ability to plastically deform without fracturing. Hence, nanostructured diamond films with small diamond grains from about 5 to 100 nm embedded in an amorphous carbon phase could be of significant value. Even though these films have a hardness of ~80% of natural diamond, they are smoother and have higher fracture toughness [9].

Nucleation of diamond is an important step in the growth of diamond thin films, because it strongly influences the diamond growth process, film quality, and morphology. Generally, seeding or abrading with diamond powder or immersing in diamond paste containing small crystallites processed in an ultrasonic bath enhances nucleation. The most promising in situ method for diamond nucleation enhancement is a negative substrate biasing during the initial stage of deposition. Figure 2 shows the effects of enhancing diamond deposition bu abrading and seeding the surface with natural diamonds.

The substrate temperature has a profound effect the crystal size and morphology of the diamond films. Using the vertical arrangement the micro-cutting tools are placed concentrically within the filament coils. With this configuration, the temperature varies significantly from the middle to the ends of the filament. This results in variable temperature at the substrate. The structure and the morphology of diamond films are thus affected quite significantly. An analysis of temperature distribution along the coiled filament is required. Filament temperature measurements are carried out using a two-color optical pyrometer at various positions along the filament. The temperature variation at various positions along the tool can be used to calculate stress in the thin diamond film. Ager and Drory [10] investigated residual biaxial stress in diamond films grown on titanium alloys by Raman spectroscopy and developed a general model, which quantitatively describes the relations between singlet and doublet phonon scattering and the biaxial stress, σ, as follows:

$$\sigma = -0.567(v_m - v_0) \tag{1}$$

where v_0 is 1332 cm^{-1} and v_s is the observed maximum of the singlet phonon in the spectrum. For the tools used in this paper, biaxial stresses along the cutting potion of the micro-tool were calculated to be −3.4, −2.3, and −1.7 GPa in compression.

This paper discusses the use of thin diamond coatings on the performance of micro-cutting tool machining Ti6Al4V alloy that are predominantly used for machining medical devices and instruments. The paper describes a computational analysis of machining parameters to show how using diamond-coated micro-tools can reduce machining temperature and associated phenomena.

1.3 Burr formation using micro-tools

Burr formation causes dimensional distortions on the component that presents a challenge to the assembly and handling in sensitive locations on the workpiece and damages the subsurface of the material from the deformation associated due to the exit of the cutting tool from the workpiece. It is estimated that 2–8% of the manufacturing costs for a major assembly component in the automotive industry results from the removal of burrs or prior changing of tools due to over-ridging. Moreover, de-burring operations cost American companies billions of dollars annually, and it is a production headache that frequently causes bottlenecks in production and refinishing processes. In order to effectively address burr prevention, the entire “process chain” from design to manufacture must be considered to integrate all the elements affecting burrs, from the part design, including material selection, to the micro-machining process itself. When implementing burr-minimized production or metal-cutting operations, two main factors must be taken into account: firstly, the use of burr minimizing tools and secondly, the implementation of optimum process parameters [1].

There are three burr types produced in micro-drilling operations on stainless steel parts: small uniform exit burr with cap (type I), large uniform (very thin) exit burr with cap (type II), and crown burr (type III). In general, burr size depends on several cutting conditions including cutting speed and feed rate. It is confirmed well in the drilling burr control chart that the type of burr produced and burr height depends on the feed rate and the cutting (rotational) speed. For example, crown burrs of 500 μm in height are produced for maximum values of these both cutting parameters. Another approach to

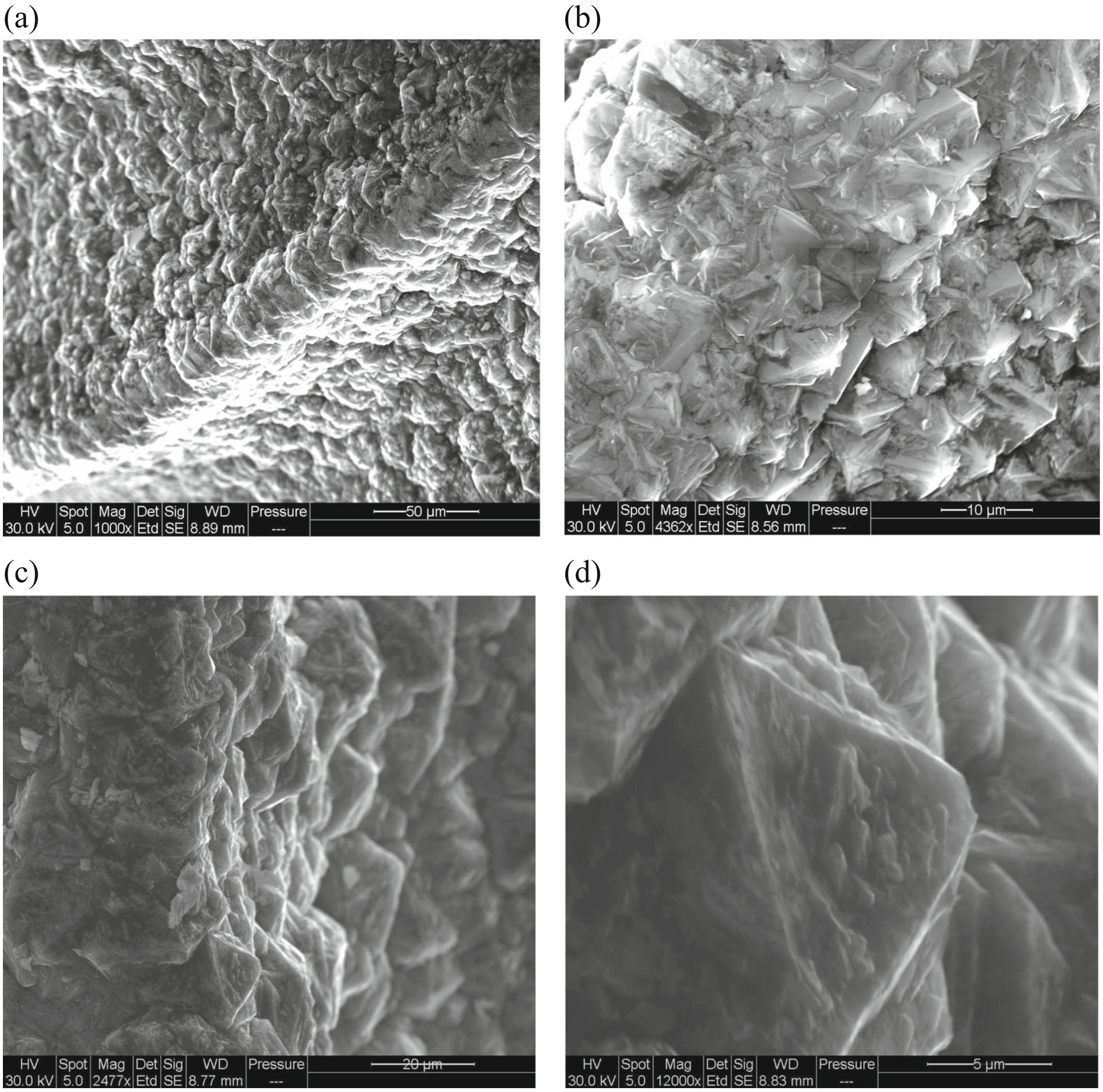

Fig. 2 Diamond nucleation on the surface of a tungsten carbide micro-cutting tool showing **a** diamond structure at the cutting edge of the tool; **b** magnified image of the crest of the cutting tooth; **c** flank face of the cutting tooth; and **d** individual diamond grain showing trigonal symmetry

minimizing burr formation in micro-drilling operations involves ultrasonic vibratory technique, which modifies material deformation/fracture conditions during the drilling process [1–4].

Ball-style miniature brushes that are highly specialized abrasive tools are used for specialized surface processing including de-burring, edge-blending, plateau honing and deglazing of critical metal surfaces. They contain small abrasive globules that are mounted to flexible filaments. Micro-milling with tungsten carbide tools is a proven and effective process for producing complex structures such as molds and micro-fluidics that are characterized by high aspect ratios and high geometrical complexity but typically rather moderate demands on surface quality. But, in many other applications, the surface quality is vital for the proper functionality of micro-components. For example, molds for micro-injection molding process need surface roughness better than Rz = 1 μm in order to guarantee removing the part from the mold cavity. Some practical observations are collected when the conventional milling process is downscaled to micrometer dimensions. In particular, the tendency is that the surface quality is better for harder materials but the burrs occur more frequently in the hardened state of steel components. Moreover, the groove walls slope away in the hardened state due to high residual stresses, which in turn, are released during the cutting process. In case of producing micro-slots in an Al6061-T6 aluminum alloy using micro-mills fabricated using micro-EDM, severe deformation of the 5-μm thin wall occurred causing the lack of flow within the micro-fluidic system. This unacceptable result is explained by unexpected vibration and/or lateral bending caused by cutting forces. Another problem occurring in micro-milling of micro-thinwalled structures concerns undesirable burrs, which are usually produced in conventional milling processes. In general, preventing or eliminating burrs is a very complex technological task that needs integration of many activities such as careful choice of tools, machining parameters, tool paths, or special work materials and part designs. In fact, most burrs can be prevented or minimized with the appropriate simulation of the machining parameters before cutting takes place and using the appropriate process controls after during cutting [1–4].

2 Computational analysis

As the cutting force/thrust force ratio changes, the stability of the process also changes. The use of diamond tools to reduce temperatures and to reduce cutting and thrust forces seem attractive to micro-machining titanium alloys and other difficult-to-machine materials. The minimum chip thickness is a measure of how effective micro-tools are and has been analyzed using methods including cutting force periodicity [11], stress ratio derived from cutting and thrust forces [12], transition from interfacial sliding to micro-cutting [13], neutral point analysis [14, 15], effects of surface roughness [16], relationships between the friction coefficient, tool radius, and minimum chip thickness [17], molecular dynamics' simulations [18] as well as traditional experimental approaches [19]. Owing to the requirements of producing medical implants using Ti6Al4V alloy with a defined surface quality, finite element modeling is used to simulate the effects of changing the cutting force/thrust force ratio, the ratio of feed per tooth/tooth edge radius, and their influences on chip formation and thermal effects in the micro-machining of Ti6Al4V titanium alloy, which has direct effect on surface quality and integrity.

In the finite element analysis (FEA), the material is represented using a continuum mechanics approach where the chemistry of the machined layers and tools, crystal lattices, and grain sizes are neglected and the material is considered to be a continuum. The number of nodes are determined arbitrarily and do not represent features of the material. The mesh parameters are set up in such a way that they determine the sensitivity of the material during the simulation by using a finer mesh when small feeds or depths of cut are used to capture features associated with machining at the micro-scale. FEA can be split into three groups: Lagrangian, Eulerian, and arbitrary Lagrangian-Eulerian methods. Lagrangian FEA is based on the assumption that the mesh is attached to the workpiece material and it moves with the material. Owing to the fact that the elements change shape it is often necessary to use re-meshing to restore distorted elements and that adaptive re-meshing is more commonly used. Eulerian FEA involves a workpiece material which flows through the pre-set mesh fixed in space. There is no element distortion using this method. However, chip formation cannot be modeled and only steady-state problems can be analyzed. Owing to the advantages and disadvantages of both methods, a combination of the two called arbitrary Lagrangian-Eulerian approach is more frequently used.

The model used in the computational analysis of chip formation and thermal analysis at the micro-scale is a three-dimensional Lagrangian-Eulerian-formulated finite element model, which is an explicit dynamic model that is thermo-mechanically coupled specifically used for micro-machining operations. The model uses adaptive re-meshing capable of finite resolutions at multiple-length scales to incorporate cutting edge radius, the secondary shear zone, and chip loading effects. Multiple body deformation simulates tool-workpiece interactions in addition to transient thermal analyses. Finite deformation kinematics and updated stress conditions have been formulated by Third Wave Systems™ in their AdvantEdge™ FEA software package that include balancing linear momentum and calculating thermal conditions using the second law of thermodynamics.

In order to use the finite element model to simulate the conditions of micro-machining Ti6Al4V titanium alloy, an appropriate material model is required to simulate micro-machining conditions. For this reason, a custom power law constitutive material model was used.

2.1 Constitutive material model

Third Wave Systems' AdvantEdge™ FEA software utilizes a custom power law constitutive material model incorporating strain hardening effects, strain rate sensitivity, thermal softening effects, and a damage model. Thus,

$$\sigma\left(\varepsilon^{p},\dot{\varepsilon},T\right)=g(\varepsilon^{p})^{*}\Gamma\left(\dot{\varepsilon}\right)^{*}\Theta(T) \tag{2}$$

where σ is the stress as function of strain hardening, strain rate sensitivity and temperature, $g(\varepsilon^{p})$ accounts for strain hardening, $\Gamma(\dot{\varepsilon})$ accounts for strain rate sensitivity, and $\Theta(T)$ accounts for thermal softening of the cut material.

Strain hardening shows the dependence of the flow stress on strain and is incorporated into the finite element model as:

$$g(\varepsilon^{p})=\sigma_0\left(1+\frac{\varepsilon^{p}}{\varepsilon^{p}_{0}}\right)^{\frac{1}{n}}\text{if}\,\varepsilon^{p}<\varepsilon^{p}_{\mathrm{cut}} \tag{3}$$

$$g(\varepsilon^{p})=\sigma_0\left(1+\frac{\varepsilon^{p}_{\mathrm{cut}}}{\varepsilon^{p}_{0}}\right)^{\frac{1}{n}}\text{if}\,\varepsilon^{p}\geq\varepsilon^{p}_{\mathrm{cut}} \tag{4}$$

where σ_0 the initial yield stress, ε^{p} is the plastic strain, $\varepsilon_0{}^{p}$ is the reference plastic strain, $\varepsilon_{\mathrm{cut}}{}^{p}$ is the cut-off strain, and n is the strain hardening exponent. Thermal softening parameters have been defined using the following equations:

$$\Theta(T) = c_0 + c_1 T + c_2 T^2 + c_3 T^3 + c_4 T^4 + c_5 T^5, \text{if } T < T_{\text{cut}} \tag{5}$$

$$\Theta(T) = \Theta(T_{\text{cut}})\left(1 - \frac{T - T_{\text{cut}}}{T_{\text{melt}} - T_{\text{cut}}}\right), \text{if } T \geq T_{\text{cut}} \tag{6}$$

where c_0 to c_5 are coefficients of the polynomial fit, T is the temperature, T_m is the melting temperature, and T_{cut} is the linear cutoff temperature. Strain-rate sensitivity is presented as the dependence of the flow stress on strain defined using the following equations:

$$\Gamma(\dot{\varepsilon}) = \left(1 + \frac{\dot{\varepsilon}}{\dot{\varepsilon}_0}\right)^{\frac{1}{m_1}}, \text{if } \dot{\varepsilon} = \dot{\varepsilon}_t \tag{7}$$

$$\Gamma\,\dot{\varepsilon} = \left(1 + \frac{\dot{\varepsilon}}{\dot{\varepsilon}_0}\right)^{\frac{1}{m_2}} \left(1 + \frac{\dot{\varepsilon}_t}{\dot{\varepsilon}_0}\right)^{\left(\frac{1}{m_1} - \frac{1}{m_2}\right)} \text{if } \dot{\varepsilon} > \dot{\varepsilon}_t \tag{8}$$

where $\acute{\varepsilon}$ is the strain rate, $\acute{\varepsilon}_0$ is the reference plastic strain rate, $\acute{\varepsilon}_t$ is the strain rate of the transition between the high and low strain sensitivity, and m_1 and m_2 are the low and high strain-rate sensitivity indices, respectively.

The damage model is expressed using the equation:

$$D = \sum_i \frac{\Delta\varepsilon_i^p}{\varepsilon_{fi}^p} \tag{9}$$

where D is the dimensionless cumulative damage, $\Delta\varepsilon_t^p$ is the instantaneous increment of strain, and $\varepsilon^{p}{}_{fi}$ is the instantaneous strain to failure. Constants applied in the power law constitutive material model are presented in Table 2.

The numerical values shown in Table 2 reflect the works of research [20–26] conducted to capture the properties of simulating the machining of Ti6Al4V titanium alloy. However, for the experiments noted here, some constants are calculated and some selected as arbitrary measures. Therefore, caution should be observed when making absolute interpretations of the computational data presented in this paper. Subsequent analyses are focused on using the finite element modeling technique to analyze chip formation mechanisms and ensure that the correct chip formation regime is selected that will improve surface quality and integrity of the machined surfaces. The associated thermal analyses are also computed that provide an understanding of where heat is generated and how it is dissipated during machining. The analysis also shows the reader when burr formation is dominating flow rather than the formation of cut chips. In relation to chip formation, the FE analysis shows how process parameters are selected in order to avoid burr formations.

3 Finite element results

3.1 Chip formation and machining forces

Initial studies in the area of modeling of the micro-machining process established the use of FEA for simulating the micro-milling process in the down-cut milling regime [11, 16]. The geometry of the end view of the cutting edge of the micro-milling tool looks similar to the adjacent view of a standard lathe cutting tool, the difference being that one tooth of the milling cutter is simulated and the curvature of the chip formed is so small it appears as though the workpiece is perpendicular to the motion of the cutting edge of the tooth. In the practical machining process, each tooth cuts a piece of the workpiece material, but the FEA model simulates the cutting associated with one tooth in contact with the workpiece material. The validity of simulating the cutting of material using one tooth is shown in Fig. 3. The six-tooth micro-milling cutter shows the chip flow direction in addition to the local geometry of one tooth (Fig. 3a, b). Here, the flow of chip material over the flank face of a cutting edge of a single tooth can be simulated in two dimensions using the Third Wave Systems' AdvantEdge™ Finite Element Analysis software using the down-cut milling regime. The simulations presented in this paper consider on edge of one tooth of the milling cutter (Fig. 3c) and the path of material flow shown in the simulations is a replica of the material flow shown in Fig. 3d, where the flow of the chip is abruptly re-directed due to the tooth's contact between the workpiece material and the tool edge radius. The applicability of the use of the FEA modeling technique has been verified by various researchers detailed in the reference section of this paper [11–16]. A conventional force analysis was compared with computational finite element models of the micro-machining process, and the accuracy of using such analysis was validated with various materials, tool materials and coatings, and machining parameters. In terms of forces, radial (dF_r) and tangential forces (dF_t) for an elemental chip at the micro-scale are:

$$dF_r = \frac{K_t R}{\tan\alpha} K_r t_c(\theta) d\theta \tag{10}$$

$$dF_t = \frac{K_t R}{\tan\alpha} t_c \theta \, d\theta \tag{11}$$

where K_t is the average cutting pressure constant, K_r is the ratio of the radial and tangential cutting force, R is the radius of the cutting tool, α is the helix angle, θ is the angular position of the cutter, and t_c is the instantaneous uncut chip thickness given as:

$$t_c = t_x \sin\theta - \frac{N}{2\pi R} t_x^2 \sin\theta \cos\theta + \frac{1}{2R} t_x^2 \cos^2 t \tag{12}$$

Table 2 Constants applied to the power law constitutive material model

Parameter	Designation	Value	Reference
Thermal conductivity (W/(m/°C))	k	7.3	[20]
Heat capacity (J/(kg/°C))	C	580	[20]
Coefficient of thermal expansion (1/°C)	α	0.970×10^{-5}	[21]
Density (kg/m^3)	ρ	4430	[21]
Initial yield stress (Pa)	σ_0	0.98×10^9	[20]
Strain hardening exponent	n	30.9	Calculated
Reference plastic strain	ε_0^p	0.0125	[22]
Cut-off strain	$\varepsilon_{\mathrm{cut}}^p$	10^4	[22]
Coefficient	C_0	999.72	Calculated
Coefficient	C_1	−0.8785	Calculated
Coefficient	C_2	−0.0141	Calculated
Coefficient	C_3	9E−0.5	Calculated
Coefficient	C_4	−2E−0.7	Calculated
Coefficient	C_5	1E−10	Calculated
Reference temperature (°C)	T_{r}	27	Arbitrary
Cutoff temperature (°C)	T_{cut}	1000	[23]
Low-rate exponent	m_1	72	Calculated
High-rate exponent	m_2	72	Calculated
Reference strain rate (1/s)	$\dot{\varepsilon}^0$	1	[24]
Threshold strain rate (1/s)	$\dot{\varepsilon}_{\mathrm{t}}$	10^6	[25]
Young's modulus (Pa)	E_{y}	1.1E^{11}	[20]
Poisson's ratio	Pr	0.41	[20]
Coefficient	D_0	11.292	Calculated
Coefficient	D_1	−0.0114	Calculated
Coefficient	D_2	4E−0.5	Calculated
Coefficient	D_3	−5E−08	Calculated
Coefficient	D_4	−2E−10	Calculated
Coefficient	D_5	4E−13	Calculated
Damage cutoff temperature (°C)	T_{c}	500	[26]
Failure strain increment	ε_{fi}^p	0.1	Arbitrary

where t_x is the feed and N is the spindle speed in revolutions per minute. Resolving the forces into horizontal (dF_x) and vertical (dF_y) directions yields:

$$dF_x = \frac{K_t r}{\tan\alpha} t_c(\theta)(\cos\theta d\theta + K_r \sin\theta d\theta) \tag{13}$$

$$dF_y = \frac{K_t R}{\tan\alpha} t_c(\theta)(\sin\theta d\theta - K_r \cos\theta d\theta) \tag{14}$$

Integrating Eqs. 13 and 14 and finding the forces in the directions give:

$$\begin{pmatrix} F_x \\ F_y \end{pmatrix} = \frac{t_x R}{2\tan\alpha} \begin{bmatrix} P_1 & P_2 \\ P_2 & -P_1 \end{bmatrix} \begin{pmatrix} K_t \\ K_t K_r \end{pmatrix} \tag{15}$$

where

$$P_1 = \left(\sin^2\theta + \frac{N}{\pi R} t_x \frac{\cos^3\theta}{3} + \frac{t_x}{R}\left(\sin\theta - \frac{\sin^3\theta}{3} \right) \right) \Bigg|_{\theta_1}^{\theta_2} \tag{16}$$

$$P_2 = \left(\theta - \frac{\sin 2\theta}{2} - \frac{N}{\pi R} \frac{\sin^3\theta}{3} - \frac{t_x}{R} \frac{\cos^3\theta}{3} \right) \Bigg|_{\theta_1}^{\theta_2} \tag{17}$$

where K_r and K_t are constants that are material specific. From their analyses, refs. [11, 16] report that their finite element formulations of cutting forces maintained close accuracy to the closed-form solutions of forces shown by Eq. 15. Their work validated the use of finite element formulations to the solution of forces in micro-machining with milling cutters.

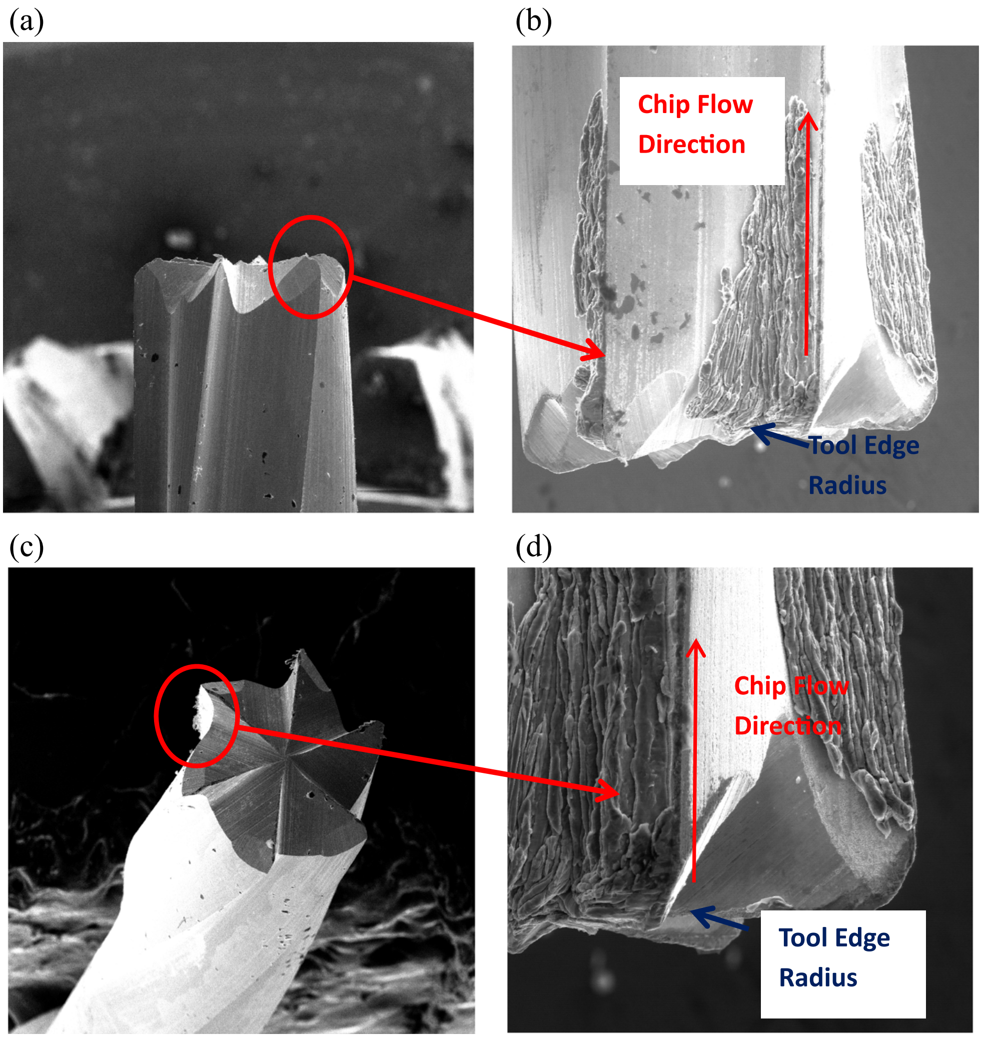

Fig. 3 Six-tooth micro-milling cutter manufactured from tungsten carbide showing: **a** the end view of the cutter, **b** a magnified image of one tooth of the cutter showing tool edge radius and the remnants of folded chip material that has adhered to the flank face of the cutting edge, **c** global view of the tips of the teeth, and **d** a magnified image of the tool edge radius and flow of the chip over the flank face of the cutting edge [26]

The machining parameters simulated in the study include variable rotational cutting speeds, variable feed/tooth, variable tool edge radii, and variable tool materials. Rotational speeds used in the simulations are 100,000, 150,000, and 200,000 rpm, respectively. The tool edge radius values used are 10 and 4 μm, respectively. The feed/tooth values used for the 10-μm tool edge radius are 10, 5, and 3.125 μm, while for the 4-μm tool edge radius, the values are 4, 2, and 1.25 μm, respectively. The tool material used for the simulations is a tungsten carbide cemented with cobalt and coated with diamond using the VFCVD technique. The cutting tool has six equi-spaced cutting teeth (Fig. 3), the rake angle of the edge of each tooth being 5° and a relief angle of 10°. The workpiece material used for the simulations was a Ti6Al4V medical-grade alloy ($\alpha + \beta$-type alloy) with the following mechanical properties: tensile strength (895–930 MPa), yield strength (825–869 MPa), elongation % (6–10%), and elastic modulus of 110–114 GPa. $\alpha + \beta$ Ti alloys include alloys with enough α- and β-stabilizers to expand the $\alpha + \beta$ phase field to exist at room temperature.

FEA analysis of the micro-machining process is shown in Figs. 4, 5, 6, 7, 8, 9, 10, 11, and 12 and Tables 3, 4, 5, 6, 7, and 8. When analyzing the results obtained for chip formation and temperature as shown in Figs. 4, 5, 6, 7, and 8, it is noted that there is a change in the chip shape as the ratio of feed per tooth (depth of cut) and tool edge radius (f_{tooth}/t_r) changes. Furthermore, as the uncut chip thickness is decreased the bending moment acting at the root of the chip changes the direction of the cut chip. For a ratio of feed per tooth and tool edge radius ~1, the bending moment acts at the chip root, moving the chip away from the tool. As the ratio of feed per tooth/tool edge radius is decreased to 0.5 ($f_{\text{tooth}}/t_r = 0.5$), the bending moment is absent and the chip moves vertically in an upward direction. As the ratio of the feed per tooth/tool edge radius is further decreased to ~0.3 (f_{tooth}/t_r ~0.3), an opposite bending moment bends the chip towards the cutting tool. These

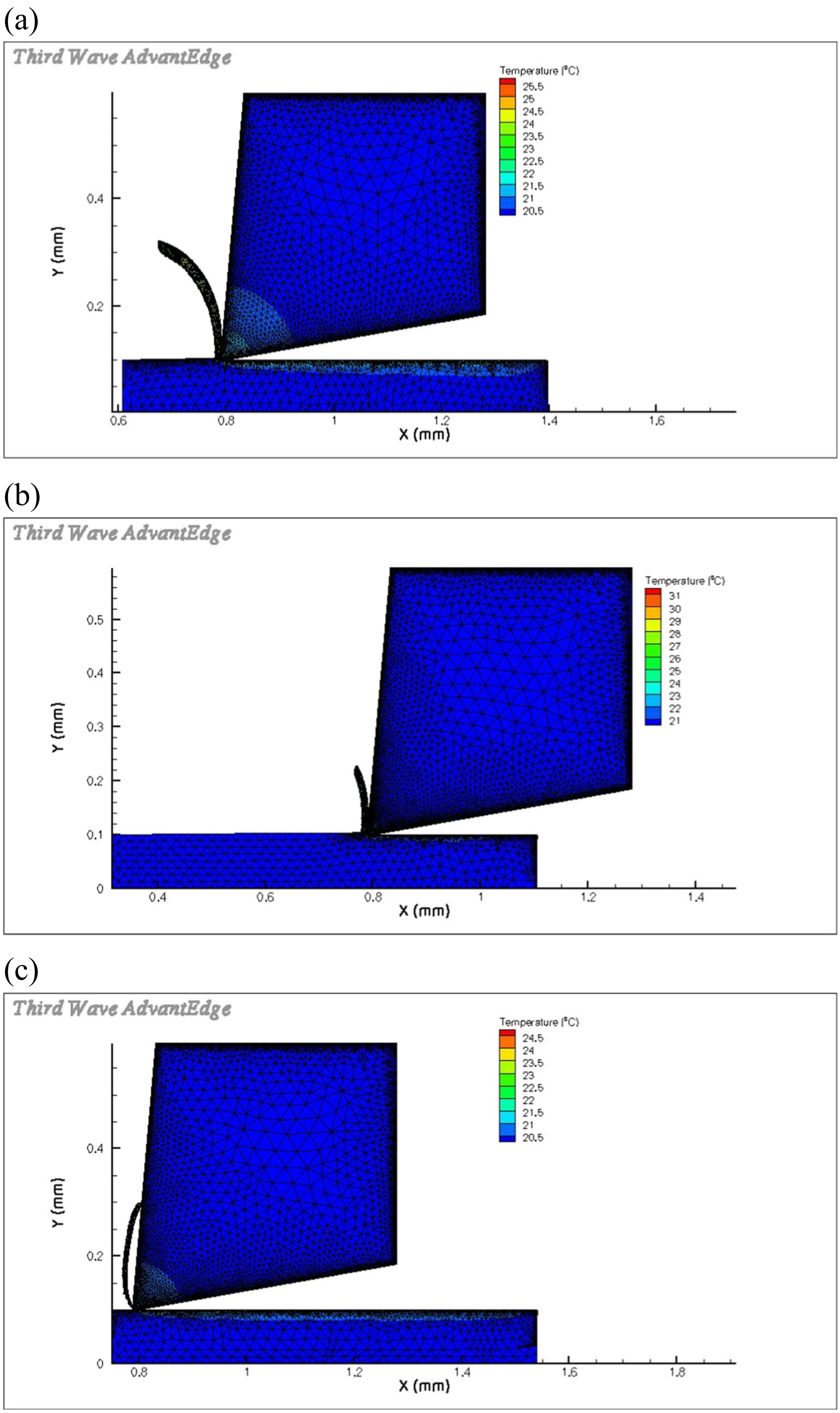

Fig. 4 Contour comparison for 10 μm tool edge radius cutting tooth machining at **a** 10, **b** 5, and **c** 3.125 μm feed per tooth using a VFCVD diamond-coated cutting tool. The spindle speed is 100,000 rpm, and the maximum temperature in cutting the chip is ~25.5, 31, and 24.5 °C, respectively

results are similar to those produced using uncoated cutting tools. The change in the feed per tooth/ tool edge radius ratio ($f_{\mathrm{tooth}}/t_{\mathrm{r}}$) also produces a change in the ratio of maximum cutting/thrust forces ($F_{\mathrm{C}}/F_{\mathrm{T}}$). As the chip thickness

Fig. 5 Contour comparison for 4 μm tool edge radius cutting tooth machining at **a** 4, **b** 2, and **c** 1.25 μm feed per tooth using a VFCVD diamond-coated cutting tool. The spindle speed is 100,000 rpm, and the maximum temperature in cutting the chip is ~24.5, 26.5, and 34 °C, respectively

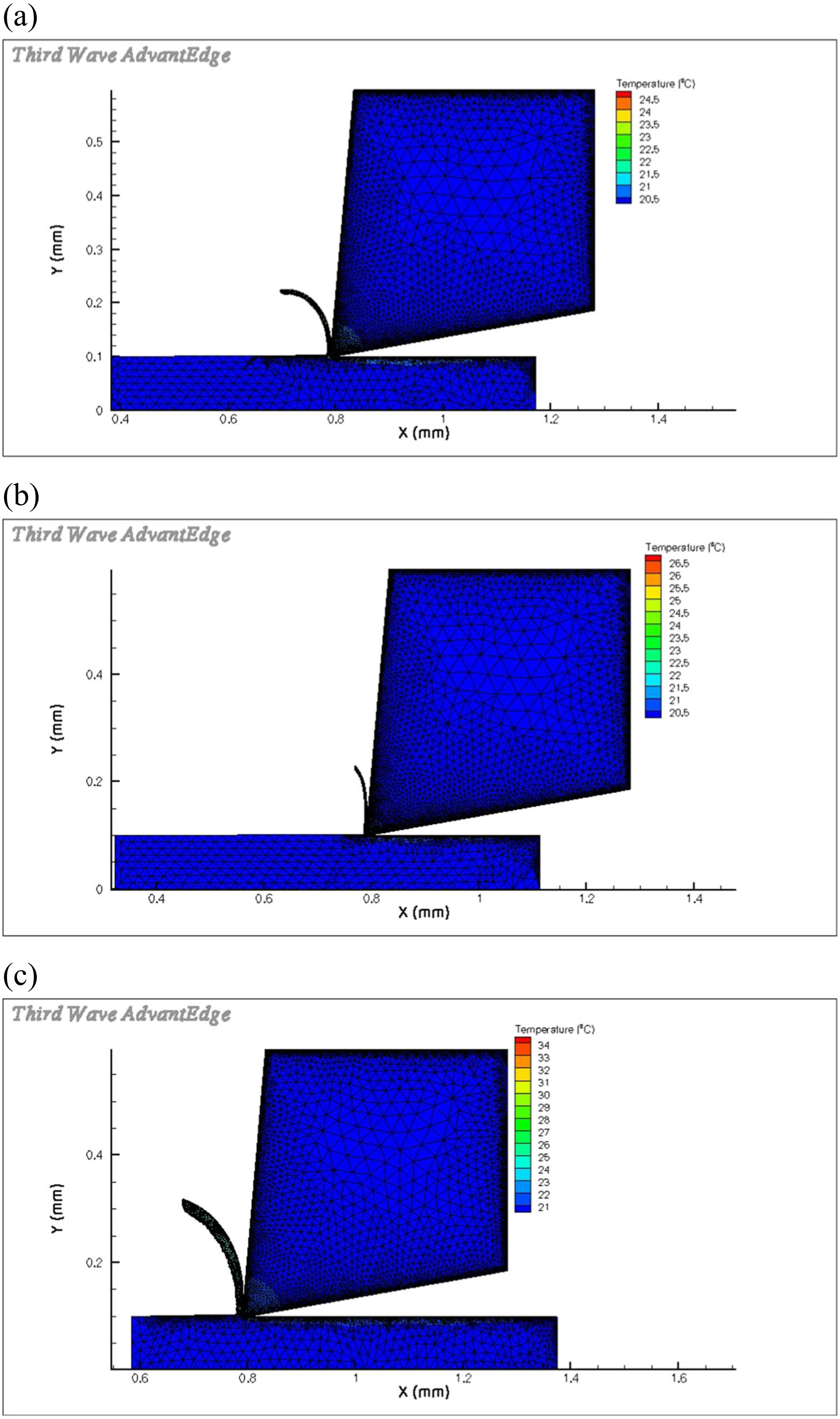

Fig. 6 Contour comparison for 10 µm tool edge radius cutting tooth machining at **a** 10, **b** 5, and **c** 3.125 µm feed per tooth using a VFCVD diamond-coated cutting tool. The spindle speed is 150,000 rpm, and the maximum temperature in cutting the chip is ~26.5, 31, and 26.5 °C, respectively

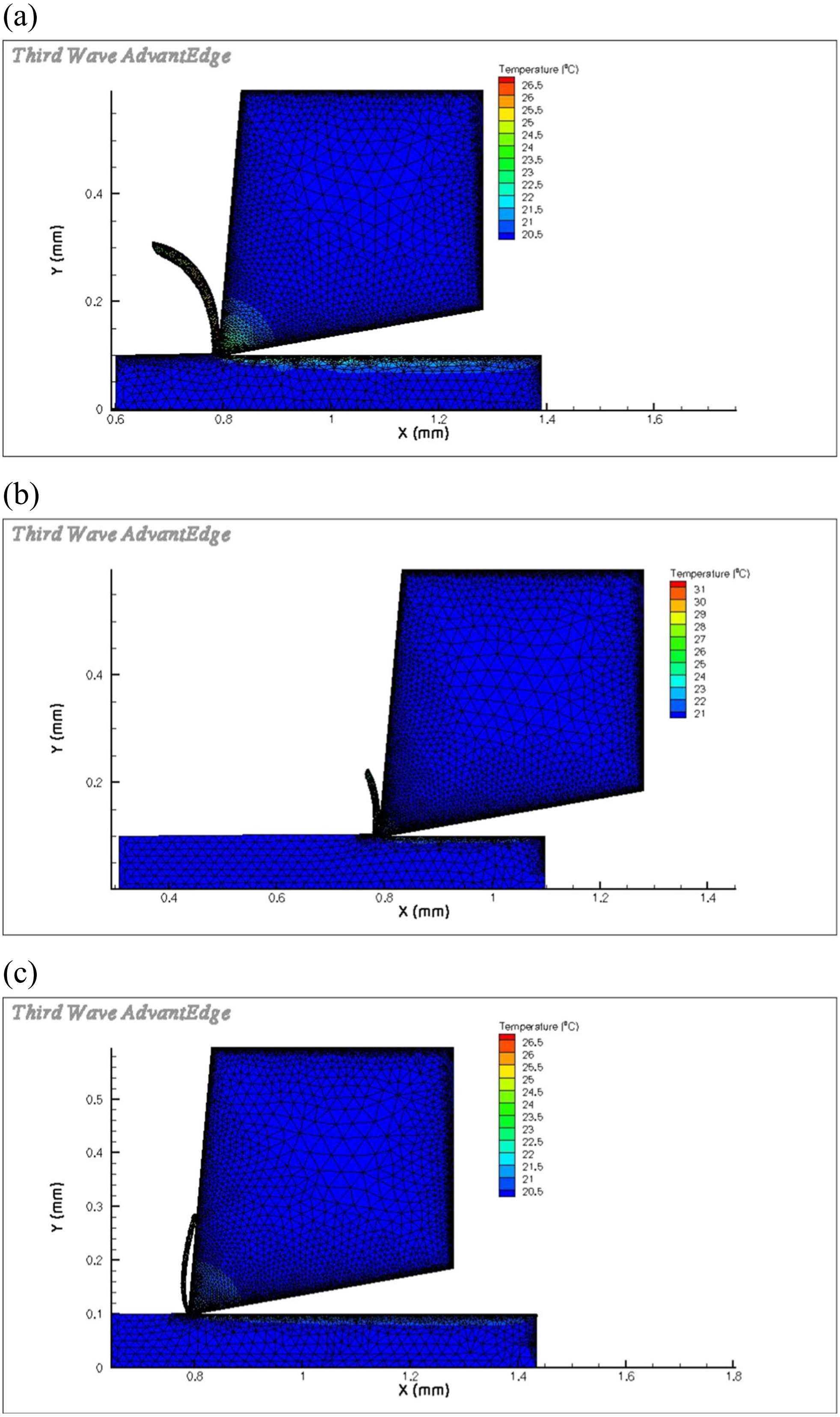

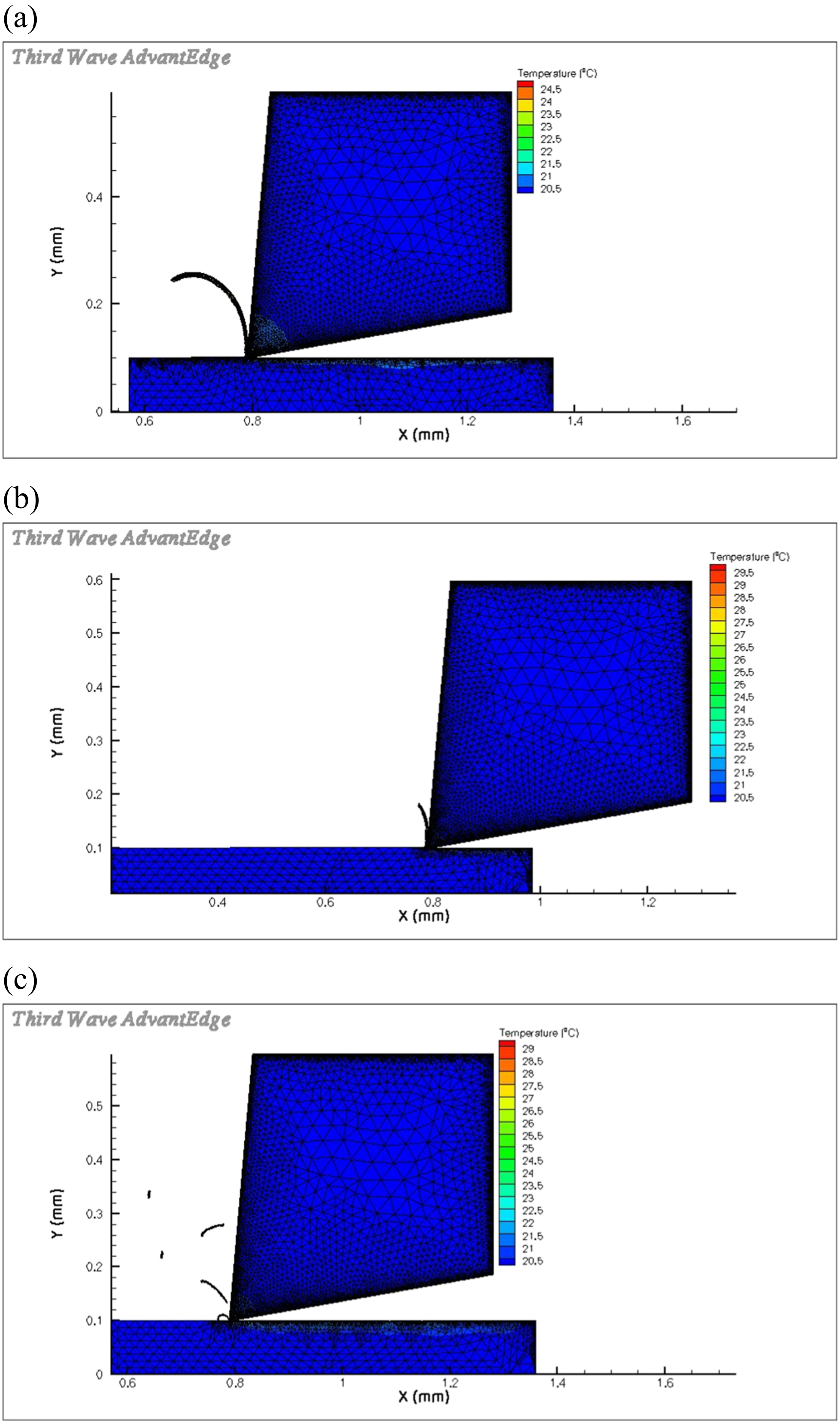

Fig. 7 Contour comparison for 4 μm tool edge radius cutting tooth machining at **a** 4, **b** 2, and **c** 1.25 μm feed per tooth using a VFCVD diamond-coated cutting tool. The spindle speed is 150,000 rpm, and the maximum temperature in cutting the chip is ~24.5, 29.5, and 29 °C, respectively

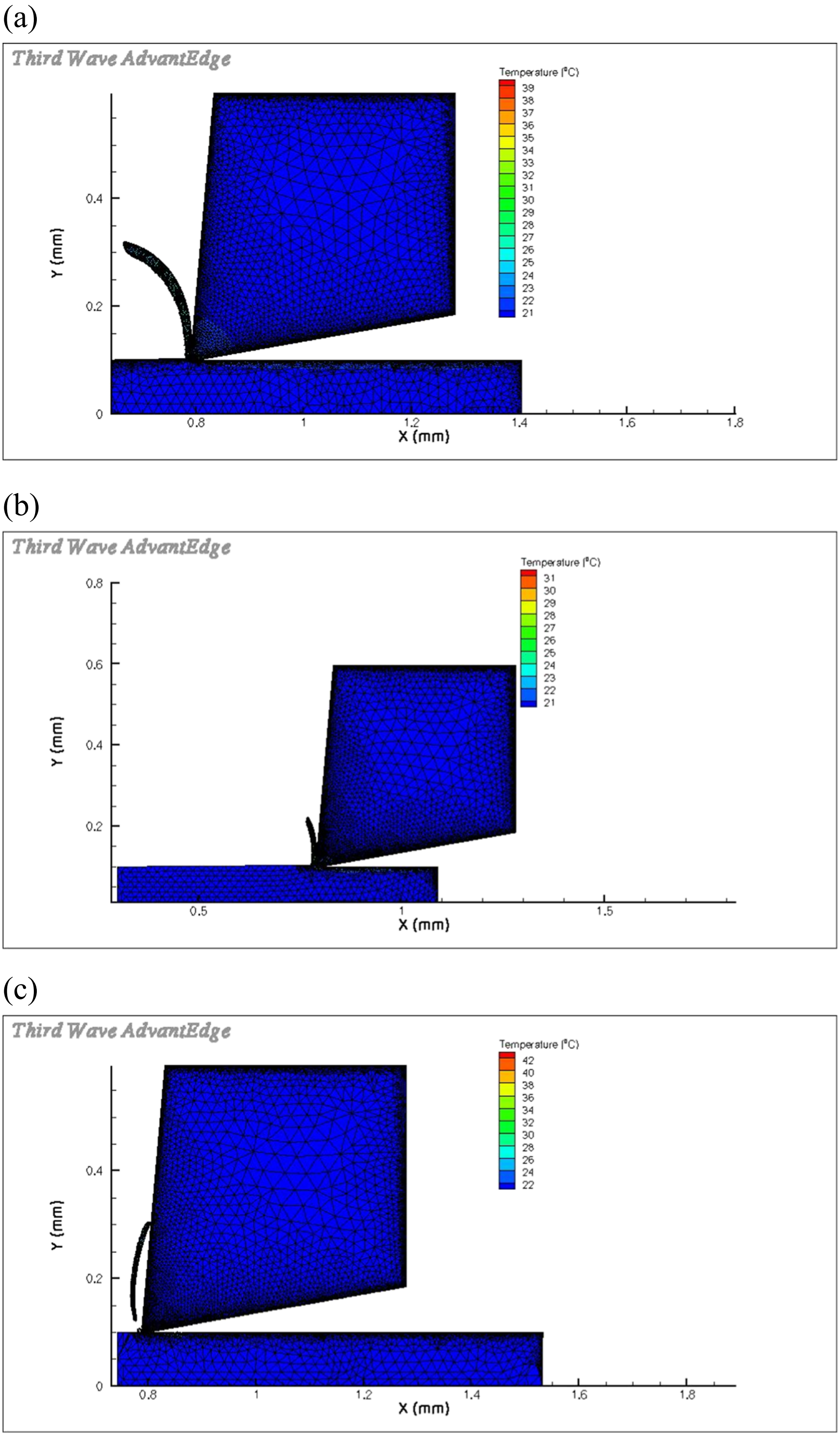

Fig. 8 Contour comparison for 10 μm tool edge radius cutting tooth machining at **a** 10, **b** 5, and **c** 3.125 μm feed per tooth using a VFCVD diamond-coated cutting tool. The spindle speed is 200,000 rpm, and the maximum temperature in cutting the chip is ~39, 31, and 42 °C, respectively

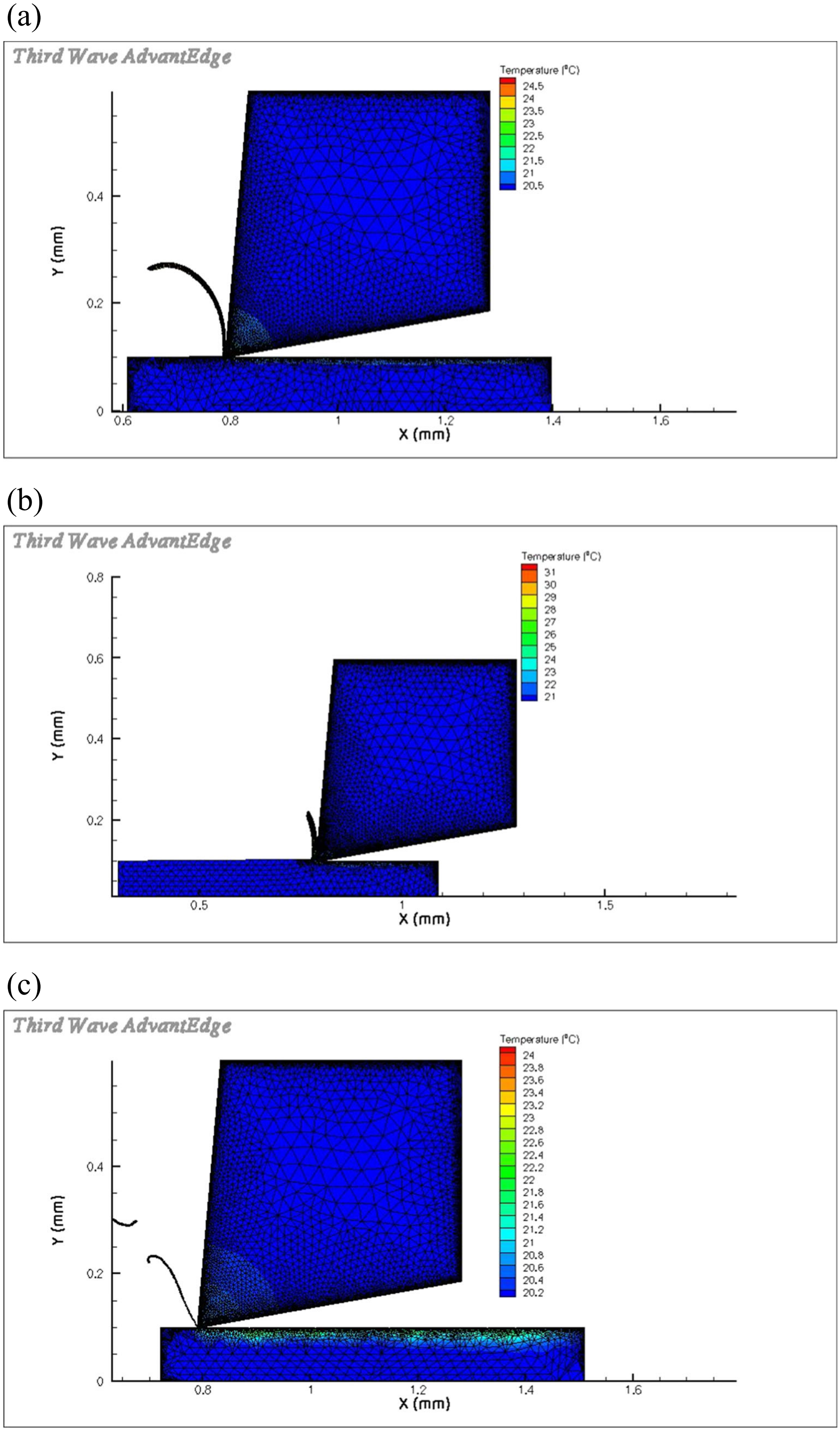

Fig. 9 Contour comparison for 4 μm tool edge radius cutting tooth machining at **a** 4, **b** 2, and **c** 1.25 μm feed per tooth using a VFCVD diamond-coated cutting tool. The spindle speed is 200,000 rpm, and the maximum temperature in cutting the chip is ~24.5, 31, and 24 °C, respectively

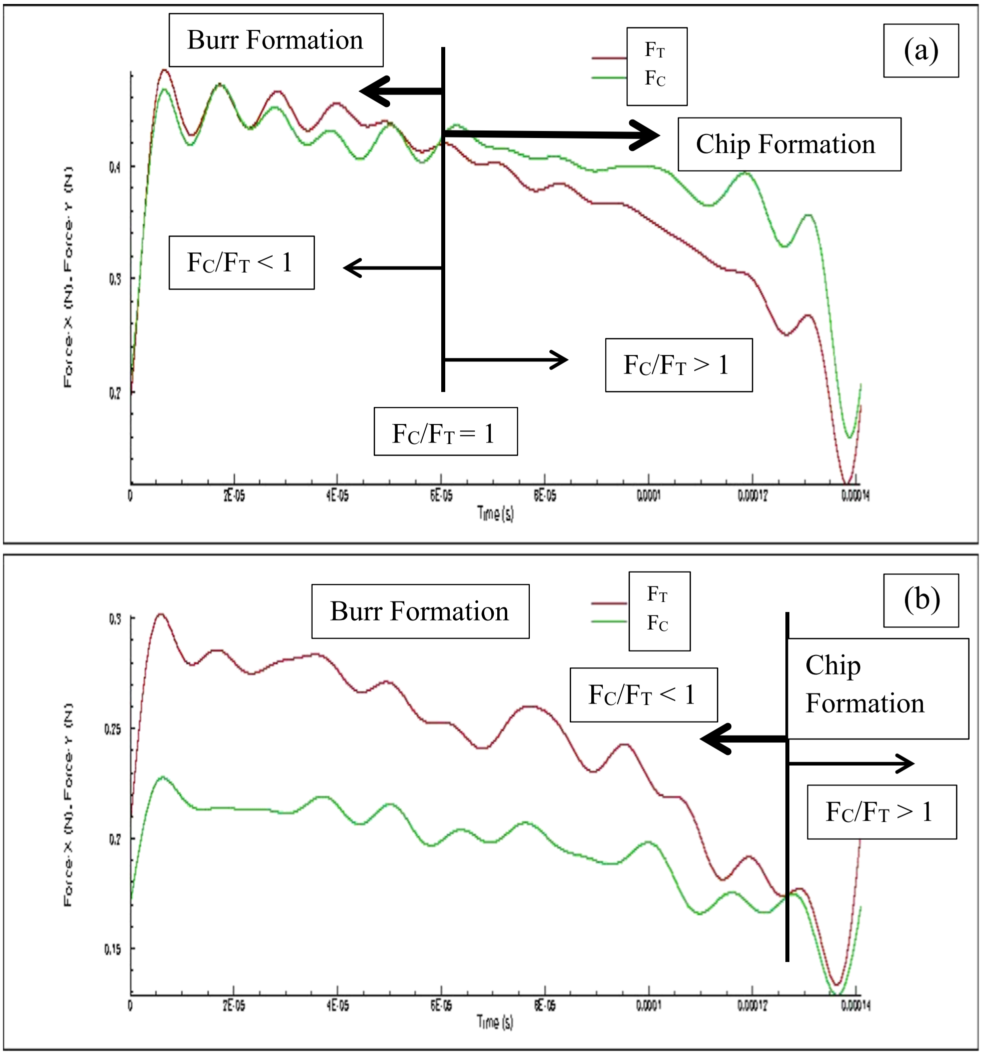

Fig. 10 Cutting and thrust forces for **a** 10 μm tool edge radius, 5 μm feed rotating at 100,000 rpm spindle speed using a VFCVD diamond-coated tool and **b** 4 μm tool edge radius, 4 μm feed rotating at 100,000 rpm spindle speed using a VFCVD diamond-coated cutting tool. The figures show the transition from burr-to-chip formation and the associated magnitude of force ratio

is decreased in the "down-cut milling" process, the cutting/thrust force ratio changes and is presented in Figs. 9, 10, 11, and 12. The transition from F_C/F_T <1 (burr formation) to F_C/F_T >1 (chip formation) defines a transition from burr-to-chip formation and is further characterized in Tables 3, 4, 5, 6, 7, and 8 using rations, F_C/F_T and f_{tooth}/t_r, for the simulations presented in this study using diamond-coated cutting tools.

The change in the ratio of cutting and thrust forces has been confirmed by other researchers [27] showing that during micro-machining processes, force components of plowing and sliding increase with the decrease in uncut chip thickness, which leads to a change in the force distribution. As opposed to macro-milling processes where the thrust force reaches a maximum level of ~30% of the maximum cutting force, the radius of the edge of the tool approaches the size of the uncut chip thickness in micro-milling processes, which causes the thrust force to become higher than the cutting force. Consequently, a change in the ratio of thrust-to-cutting force occurs. The change in force is shown to trigger the transition from cutting to plowing [27].

3.2 Cutting and thrust forces

3.2.1 Spindle speeds

When analyzing the effect of the spindle speed on cutting and thrust forces when machining Ti6Al4V titanium alloy at the macro-scale, it is apparent that there is a significant change in force when increasing the rotational speed. As the value for the rotational speed increases, the thrust force values show a direct dependence yielding higher values [28]. The rise in the thrust force with the increase in rotational speed is attributed to the adherence of the chip to the cutting tool caused by an increase in thermal energy [29]. The degree of adherence is considered to increase with the increase in speed due to the

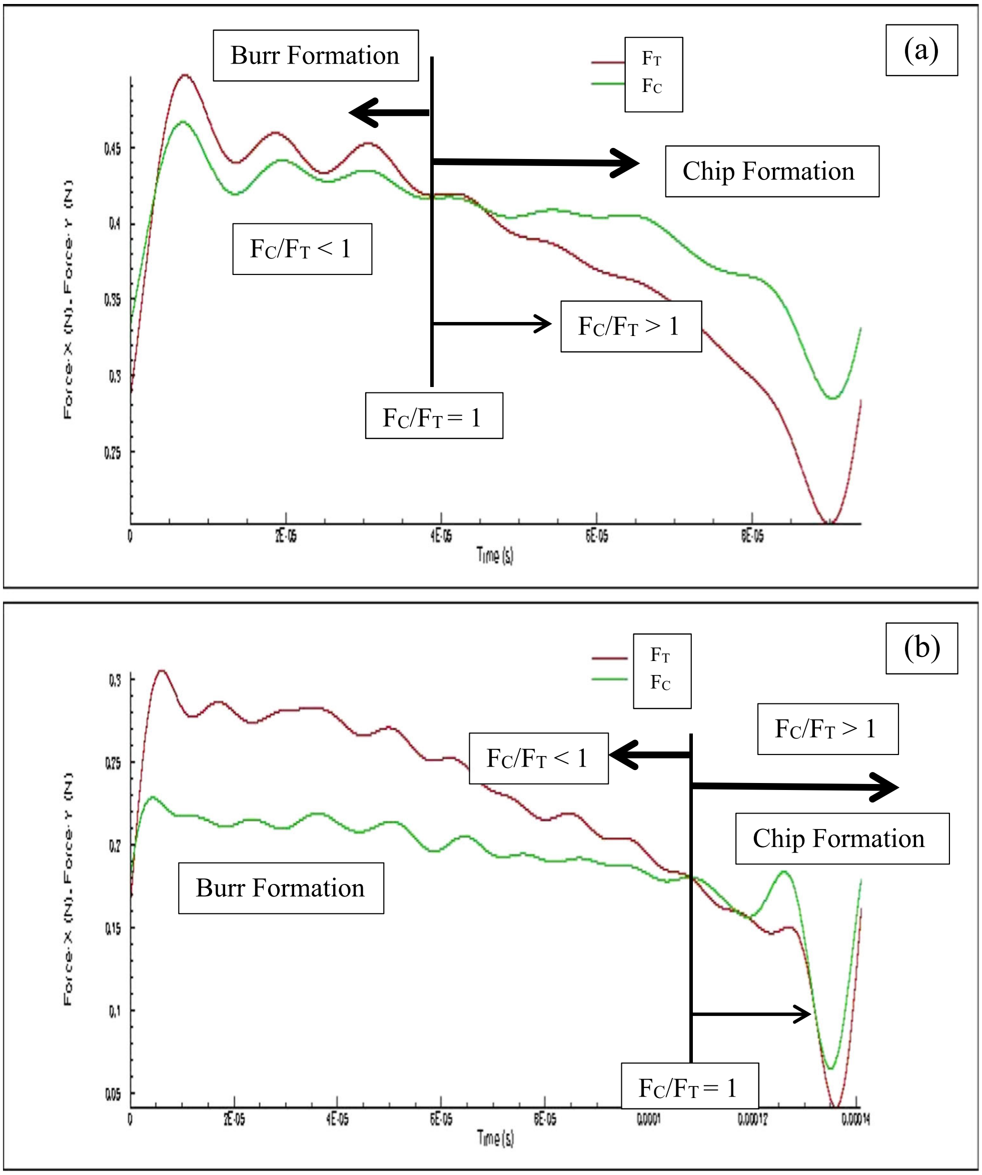

Fig. 11 Cutting and thrust forces for **a** 10 μm tool edge radius, 5 μm feed rotating at 150,000 rpm spindle speed using a VFCVD diamond-coated tool and **b** 4 μm tool edge radius, 4 μm feed rotating at 150,000 rpm spindle speed using a VFCVD diamond-coated cutting tool. The figures show the transition from burr-to-chip formation and the associated magnitude of force ratio

increase in temperature, eventually resulting in the increase in thrust force. Robinson [30] revealed that temperatures in micro-machining commonly used engineering materials are very low, and when micro-machining Ti6Al4V titanium alloy, the temperature stabilizes at ~25 °C depending upon the machining parameters. Therefore, the fact that there is a lack of sustained heat flow at high temperatures allows one to predict that the chips generated during micro-machining do not actually adhere to the cutting tool, and consequently thrust forces do not change with an increase in the rotational speed of the cutting tool. The stability in computed magnitudes of forces with the consequent change in the rotational speed is presented in Figs. 13 and 14. For the VFCVD diamond-coated tools, the forces are relatively stable at the three magnitudes of cutting feeds. For diamond-coated tools, the cutting forces are stable, while the thrust force shows some level of stability that could be attributed to difference in hardness between using tungsten carbide and diamond as the tool material.

3.2.2 Cutting feed per tooth

The influence of the feed per tooth when micro-machining Ti6Al4V titanium alloy is significant. The point at which the forces are equal is used to define the stability of the process and the recommended parameters in terms of feed per tooth, tool diameter and spindle speed [30]. It is shown (Figs. 15 and 16) that both cutting and thrust forces increase with the increase in the feed/tooth. The transition point defines three stages of machining: (A) burr formation, (B) mixed mode region, and (C) chip formation. There is a strong similarity when the results are compared with the results of Kim and

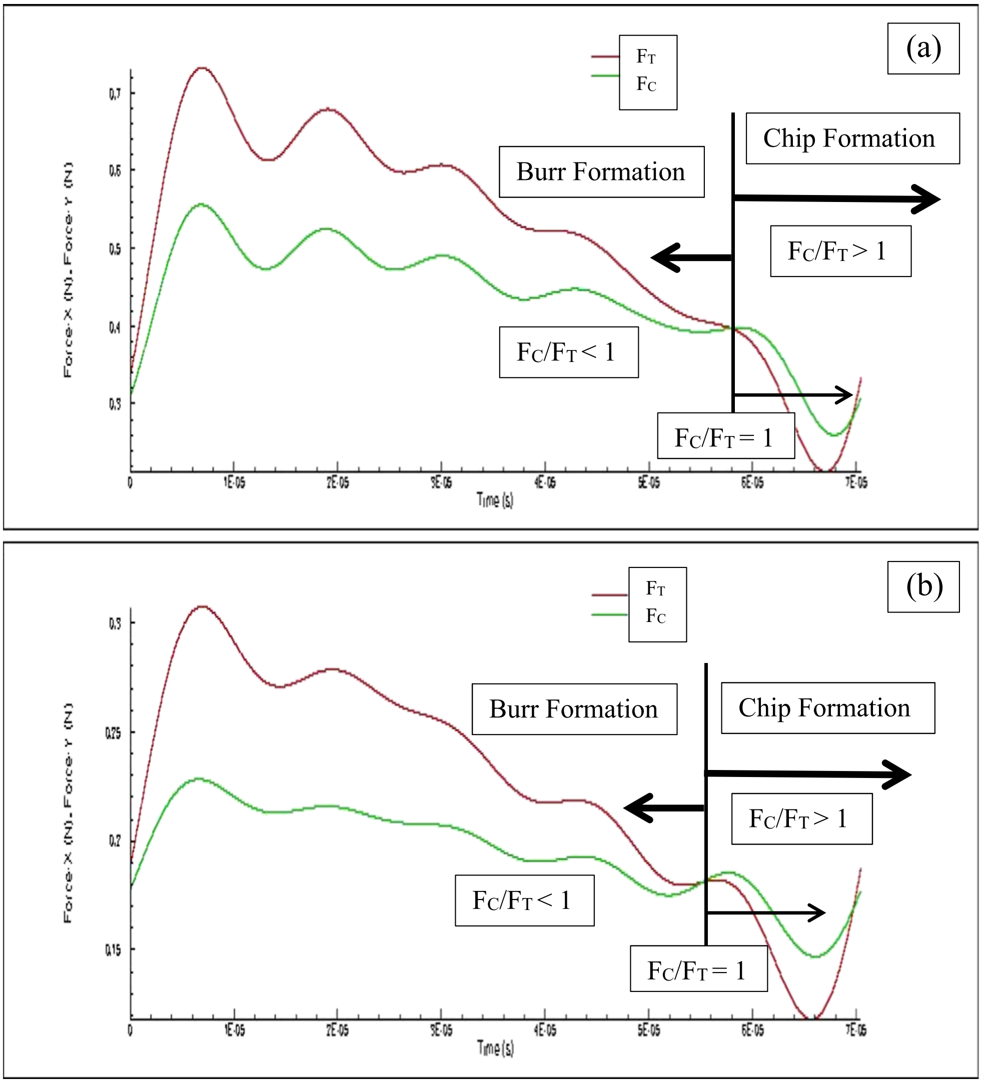

Fig. 12 Cutting and thrust forces for **a** 10 μm tool edge radius, 5 μm feed rotating at 200,000 rpm spindle speed using a VFCVD diamond-coated tool and **b** 4 μm tool edge radius, 4 μm feed rotating at 200,000 rpm spindle speed using a VFCVD diamond-coated cutting tool. The figures show the transition from burr-to-chip formation and the associated magnitude of force ratio

Kim [31] who had differentiated micro- and macro-cutting processes.

Their research shows that the trend of the force increase with the depth of cut is accounted for by three components of the force: the rake face which is the equivalent to the cutting force in macro-machining, the clearance face which is a consequence of the contact of the workpiece, and the tool clearance face due to the elastic spring back of the workpiece material and the round edge of the tool [31].

3.3 Variation in heating rate

When the change in heating rate at the point where $F_C = F_T$ is analyzed, there is a transition of forces from burr formation to chip formation. When F_C/F_T <1, burr formation is predominant and when F_C/F_T >1, the chip formation is prevalent. Figures 17, 18, 19, 20, 21, 22, 23, 24, 25, 26, 27, and 28 show that there is a drastic difference in the shape and position of the diffusion of heat around the primary shear zone. The heating rate changes direction when there is a change from burr formation to chip formation. Before the transition, i.e., when stable machining and chip formation is present, the heating rate field is located in the chip root showing that the heat will dissipate into the chip rather than into the workpiece. The heat is then taken away by the chips from the tool and workpiece. It can be seen that the highest heating rate occurs at the chip root and is concentrated in one area with no distinctive dissipation path identified. Upon crossing into the region of burr formation, the heating rate field can be seen to move away from the free surface of the chip towards the tool and under the tool into the workpiece. Rather than going into the burr the heat is partitioned into the workpiece. The partitioned heat could be considered responsible for the re-welding of the cracks in the burrs as it is pushed out of the tool-work material contact zone. It can be seen that the highest heating rate is covers a larger area below the tool as well

Table 3 Effect of the feed per tooth/tool edge radius ratio (f_{tooth}/t_r) on chip and non-chip (burr) formation with the associated force condition (VFCVD diamond-coated tool)

<table>
<tr><th>Simulation condition</th><th>Chip formation simulation (plastic strain)</th><th>Feed per tooth /tool edge ratio, (f_{tooth}/t_r)</th><th>Cutting force condition, F_C and F_T</th></tr>
<tr><td>10μm tool edge radius, 10 μm feed/tooth and 100,000 rpm spindle speed using a VFCVD diamond coated tool.</td><td>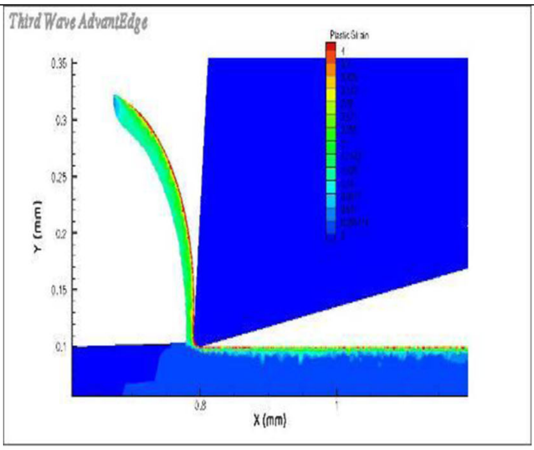
</td><td>1</td><td>$F_C > F_T$</td></tr>
<tr><td>10 μm tool edge radius, 5 μm feed/tooth and 100,000 rpm spindle speed using a VFCVD diamond coated tool.</td><td>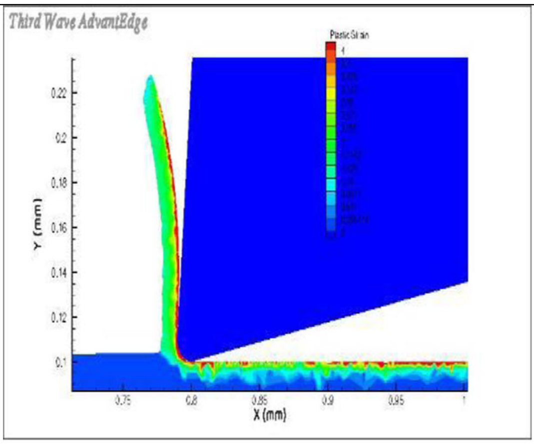
</td><td>0.5</td><td>$F_C = F_T$</td></tr>
<tr><td>10 μm tool edge radius, 3.125 μm feed/tooth and 100,000 rpm spindle speed using a VFCVD diamond coated tool.</td><td>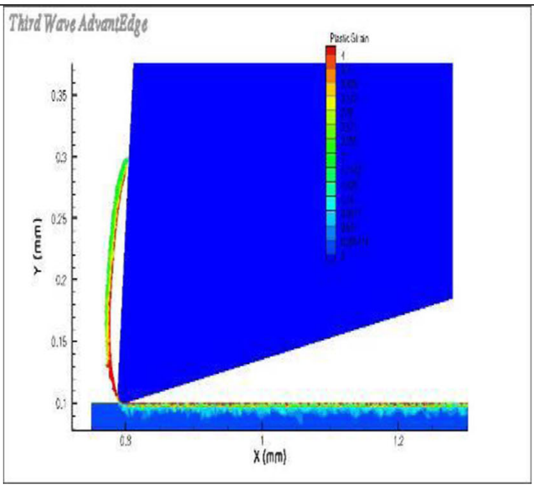
</td><td>~0.3</td><td>$F_C < F_T$</td></tr>
</table>

Simulation conditions include 10 μm tool edge radius, 10, 5, and 3.125 μm feed/tooth, and 100,000 rpm spindle speed using a VFCVD diamond-coated tool

Table 4 Effect of the feed per tooth/tool edge radius ratio (f_{tooth}/t_r) on chip and non-chip (burr) formation with the associated force condition (VFCVD diamond-coated tool)

Simulation condition	Chip formation simulation (plastic strain)	Feed per tooth /tool edge ratio, (f_{tooth}/t_r)	Cutting force condition, F_C and F_T
4µm tool edge radius, 4 µm feed/tooth and 100,000 rpm spindle speed using a VFCVD diamond coated tool.	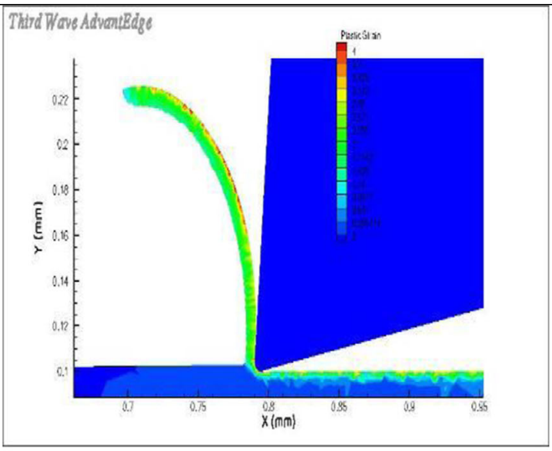	1	$F_C > F_T$
4 µm tool edge radius, 2 µm feed/tooth and 100,000 rpm spindle speed using a VFCVD diamond coated tool.	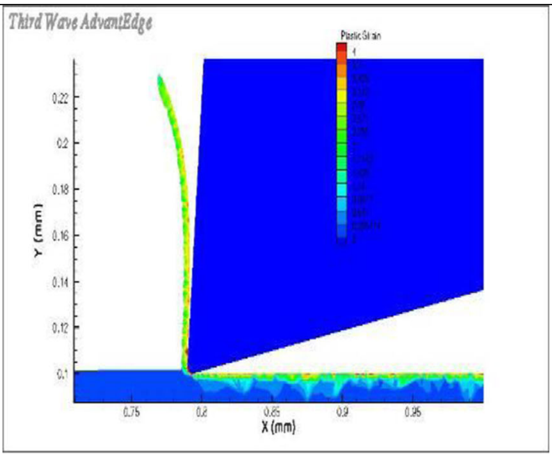	0.5	$F_C = F_T$
4 µm tool edge radius, 1.25 µm feed/tooth and 100,000 rpm spindle speed using a VFCVD diamond coated tool.	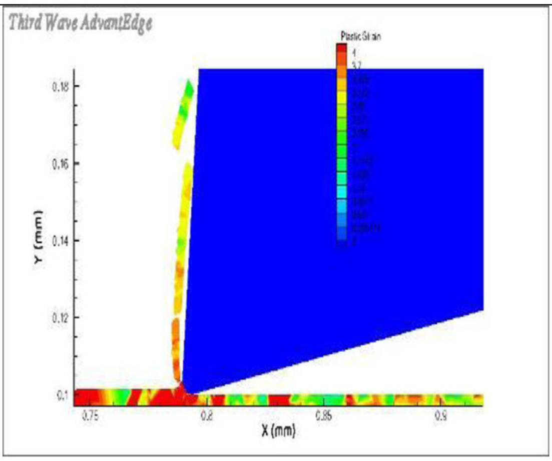	~0.3	$F_C < F_T$

Simulation conditions include 4 µm tool edge radius, 4, 2, and 1.25 µm feed/tooth, and 100,000 rpm spindle speed using a VFCVD diamond-coated tool

Table 5 Effect of the feed per tooth/tool edge radius ratio (f_{tooth}/t_r) on chip and non-chip (burr) formation with the associated force condition (VFCVD diamond-coated tool)

Simulation condition	Chip formation simulation (plastic strain)	Feed per tooth /tool edge ratio, (f_{tooth}/t_r)	Cutting force condition, F_C and F_T
10µm tool edge radius, 10 µm feed/tooth and 150,000 rpm spindle speed using a VFCVD diamond coated tool.	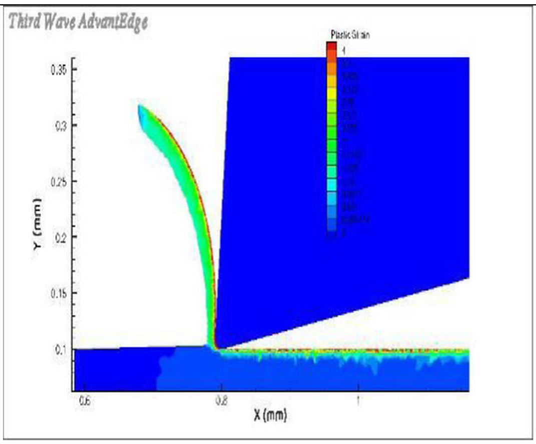	1	$F_C > F_T$
10 µm tool edge radius, 5 µm feed/tooth and 150,000 rpm spindle speed using a VFCVD diamond coated tool.	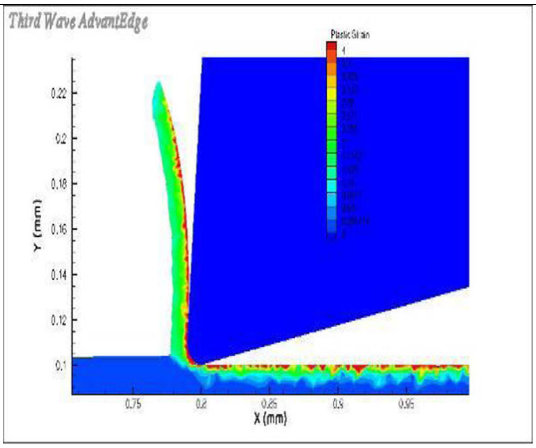	0.5	$F_C = F_T$
10 µm tool edge radius, 3.125 µm feed/tooth and 150,000 rpm spindle speed using a VFCVD diamond coated tool.	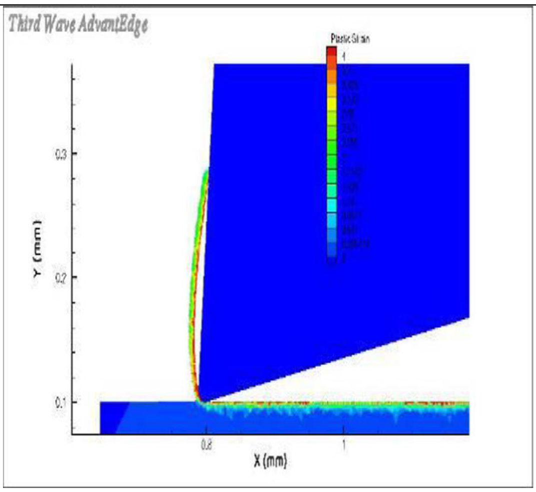	~0.3	$F_C < F_T$

Simulation conditions include 10 µm tool edge radius, 10, 5, and 3.125 µm feed/tooth, and 150,000 rpm spindle speed using a VFCVD diamond-coated tool

Table 6 Effect of the feed per tooth/tool edge radius ratio (f_{tooth}/t_r) on chip and non-chip (burr) formation with the associated force condition (VFCVD diamond-coated tool)

Simulation condition	Chip formation simulation (plastic strain)	Feed per tooth /tool edge ratio, (f_{tooth}/t_r)	Cutting force condition, F_C and F_T
4µm tool edge radius, 4 µm feed/tooth and 150,000 rpm spindle speed using a VFCVD diamond coated tool.	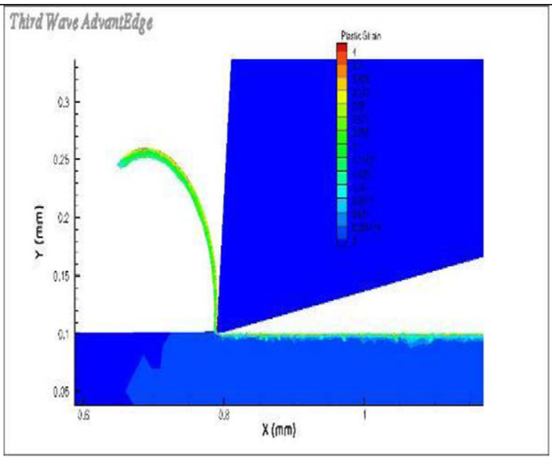	1	$F_C > F_T$
4 µm tool edge radius, 2 µm feed/tooth and 150,000 rpm spindle speed using a VFCVD diamond coated tool.	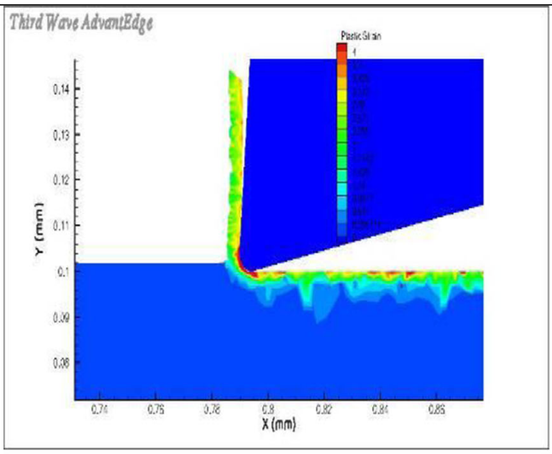	0.5	$F_C = F_T$
4 µm tool edge radius, 1.25 µm feed/tooth and 150,000 rpm spindle speed using a VFCVD diamond coated tool.	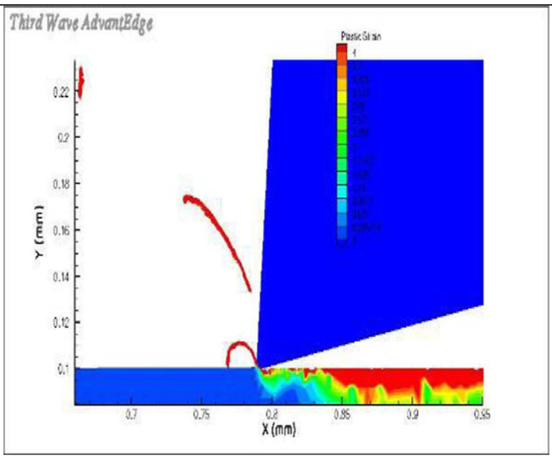	~0.3	$F_C < F_T$

Simulation conditions include 4 µm tool edge radius, 4, 2, and 1.25 µm feed/tooth, and 150,000 rpm spindle speed using a VFCVD diamond-coated tool

Table 7 Effect of the feed per tooth/tool edge radius ratio (f_{tooth}/t_r) on chip and non-chip (burr) formation with the associated force condition (VFCVD diamond-coated tool)

Simulation condition	Chip formation simulation (plastic strain)	Feed per tooth /tool edge ratio, (f_{tooth}/t_r)	Cutting force condition, F_C and F_T
10μm tool edge radius, 10 μm feed/tooth and 200,000 rpm spindle speed using a VFCVD diamond coated tool.	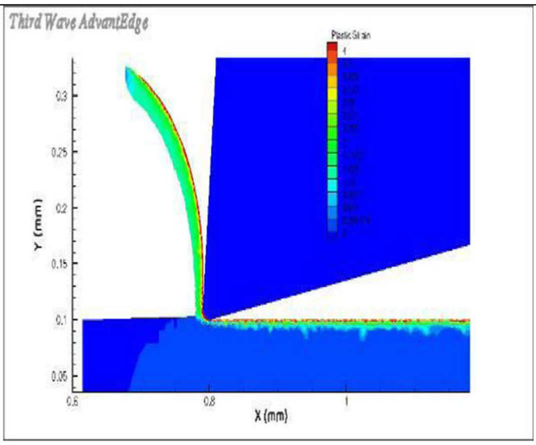	1	$F_C > F_T$
10 μm tool edge radius, 5 μm feed/tooth and 200,000 rpm spindle speed using a VFCVD diamond coated tool.	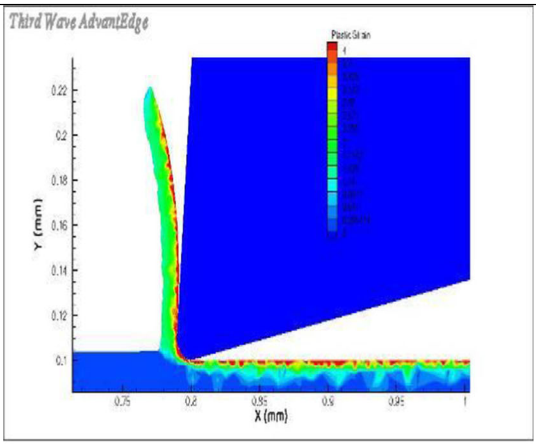	0.5	$F_C = F_T$
10 μm tool edge radius, 3.125 μm feed/tooth and 200,000 rpm spindle speed using a VFCVD diamond coated tool.	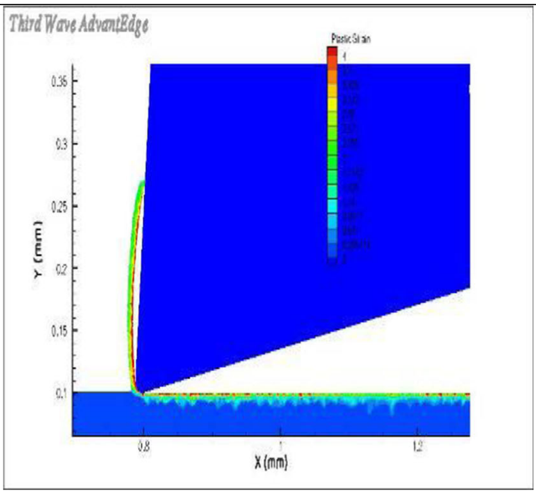	~0.3	$F_C < F_T$

Simulation conditions include 10 μm tool edge radius, 10, 5, and 3.125 μm feed/tooth, and 200,000 rpm spindle speed using a VFCVD diamond-coated tool

Table 8 Effect of the feed per tooth/tool edge radius ratio (f_{tooth}/t_r) on chip and non-chip (burr) formation with the associated force condition (VFCVD diamond-coated tool)

Simulation condition	Chip formation simulation (plastic strain)	Feed per tooth /tool edge ratio, (f_{tooth}/t_r)	Cutting force condition, F_C and F_T
4µm tool edge radius, 4 µm feed/tooth and 200,000 rpm spindle speed using a VFCVD diamond coated tool.	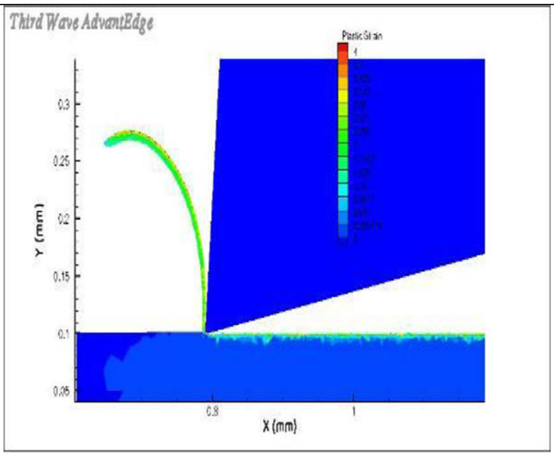	1	$F_C > F_T$
4 µm tool edge radius, 2 µm feed/tooth and 200,000 rpm spindle speed using a VFCVD diamond coated tool.	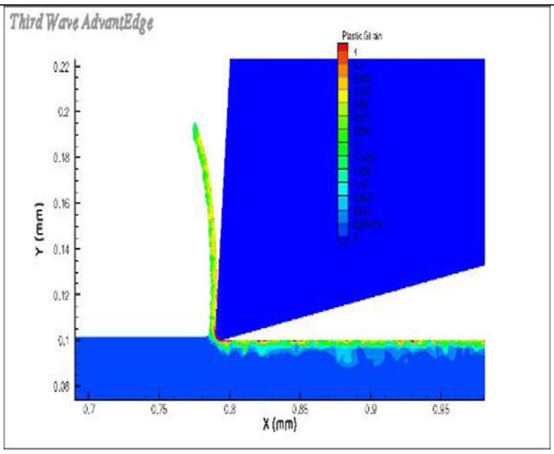	0.5	$F_C = F_T$
4 µm tool edge radius, 1.25 µm feed/tooth and 200,000 rpm spindle speed using a VFCVD diamond coated tool.	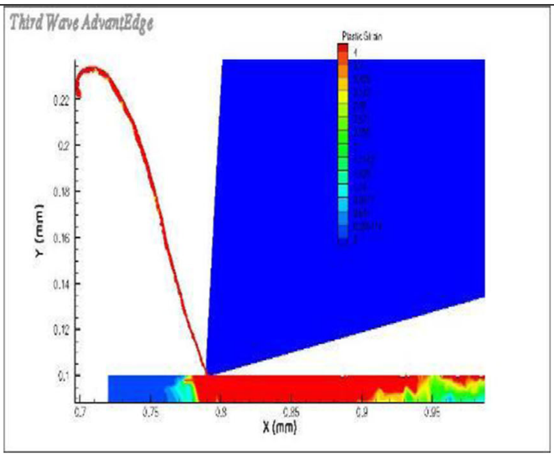	~0.3	$F_C < F_T$

Simulation conditions include 4 µm tool edge radius, 4, 2, and 1.25 µm feed/tooth, and 200,000 rpm spindle speed using a VFCVD diamond-coated tool

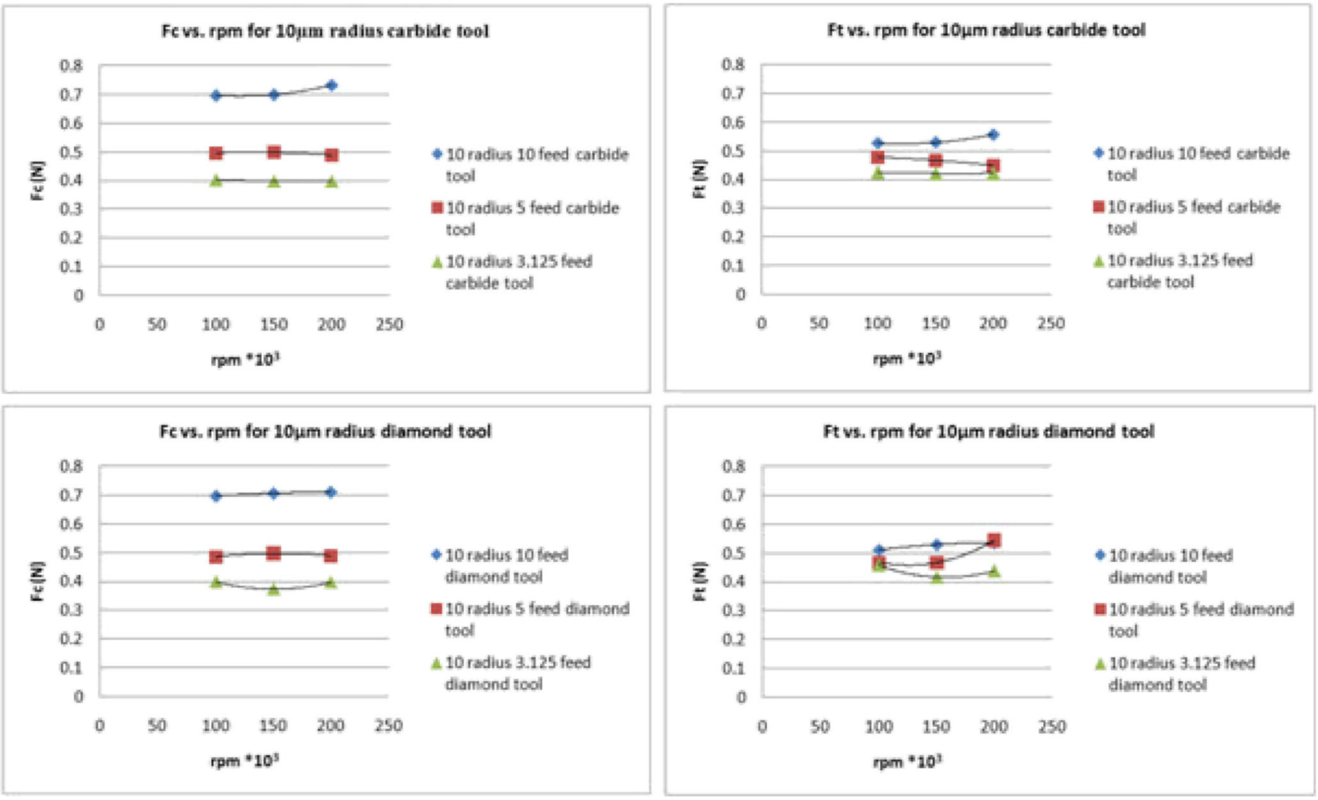

Fig. 13 Computed cutting and thrust forces as a function of spindle speed for a 10 µm edge radius cutting tool (tungsten carbide and VFCVD diamond cutting tool materials). Cutting feeds are **a** 10, **b** 5, and **c** 3.125 µm feed/tooth

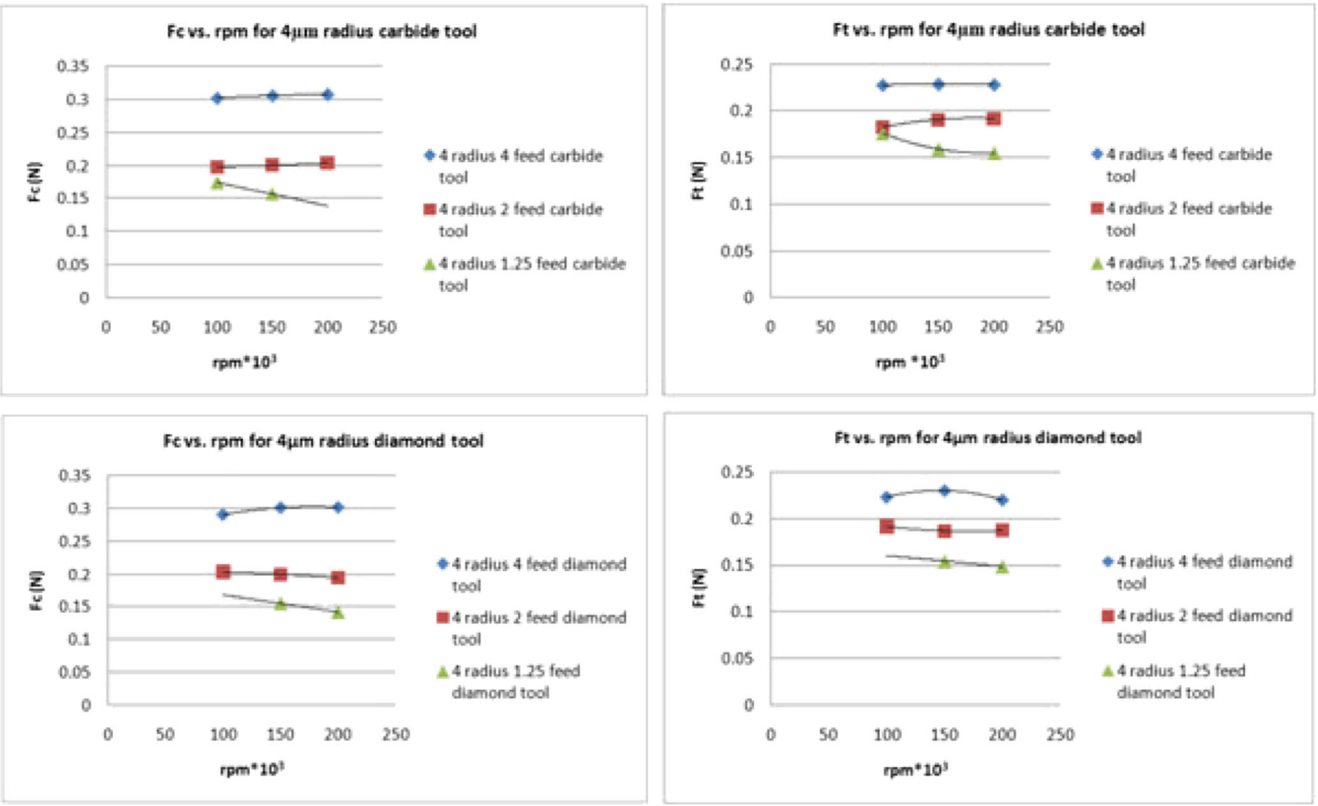

Fig. 14 Computed cutting and thrust forces as a function of spindle speed for a 4-µm edge radius cutting tool (tungsten carbide and VFCVD diamond cutting tool materials). Cutting feeds are **a** 4, **b** 2, and (c) 1.25 µm feed/tooth

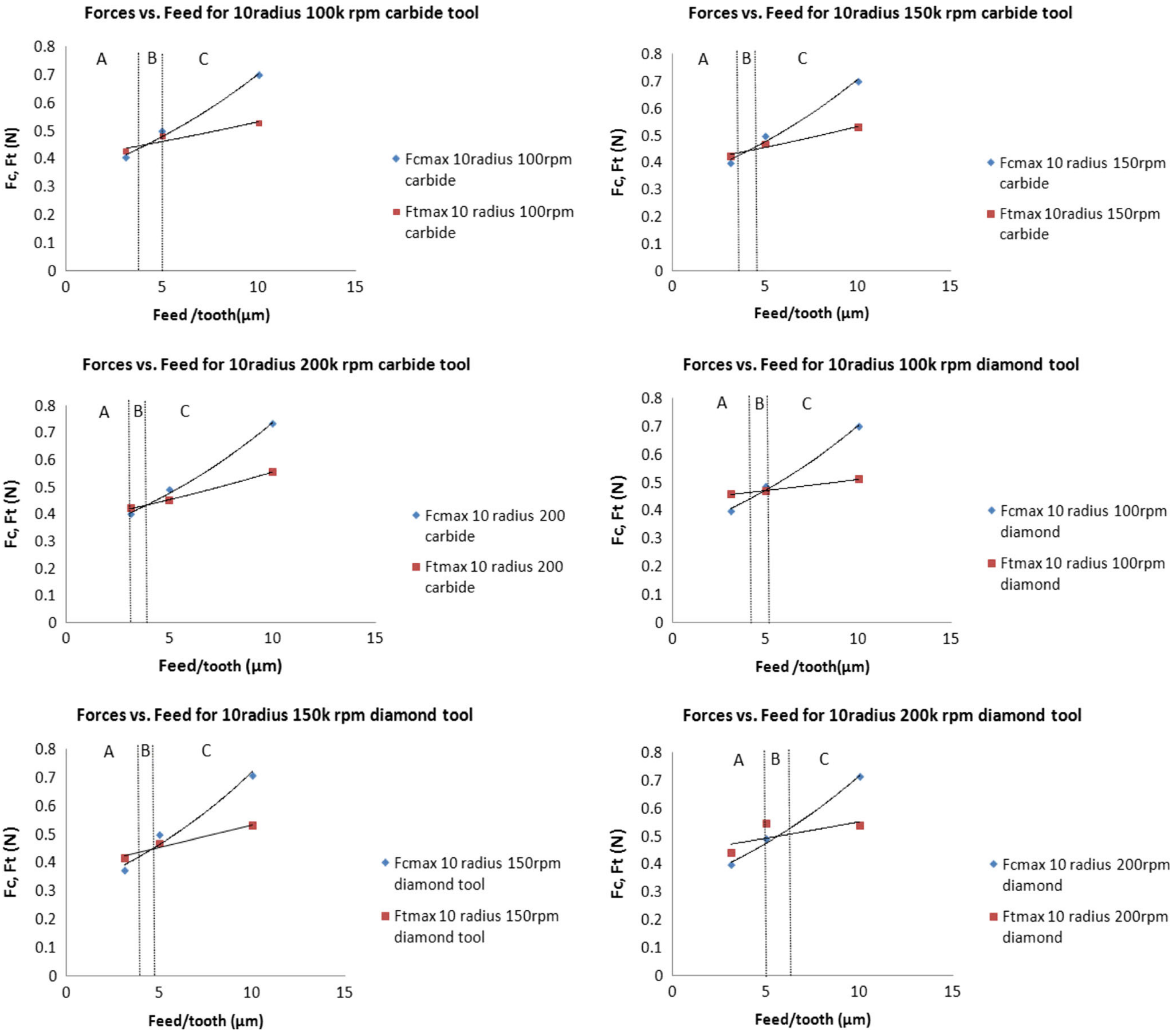

Fig. 15 Force versus feed/tooth for a 10-µm tool edge radius cutting tool at various spindle speeds and cutting tool material. **a** F_C/F_T <1 (burr formation), **b** $F_C/F_T = 1$, and **c** F_C/F_T >1 (chip formation)

as below the chip root into the bulk of the work material. This change in the position of the heat rate field is expected to occur and is in accordance with the phenomena associated with the burr-to-chip transition [30].

4 Discussion

4.1 Cutting forces and chip formation

The effect of the tool edge radius has been an important one throughout the investigations conducted in the finite element modeling of the machining process. Analysis has been conducted on the effect of edge roundness on stress and temperature when micro-machining AISI 4340 steel using carbide tools using an arbitrary Lagrangian-Eulerian method [32]. Researchers simulated material flow around the tool edge without re-meshing or using a chip separation criterion and argue that this way of conducting FEA gives better predictions for machining-induced stresses [32]. Li and Shi [33] investigated the effect of the cutting edge radius on forces, chip thickness, and tool temperature. Owing to the less-effective cutting with a large radius tool, the resulting cutting forces increase with the increase in the tool edge radius. The chip thickness is influenced somewhat by the increase in the tool edge radius showing slight increasing trend. An increasing trend for tool temperature is observed with the increase in tool edge radius. Figures 4, 5, 6, 7, 8, and 9 show similar trends. When the tool nose radius is increased from 4 µm to 10 µm, the temperature at the tool tip is slightly elevated (Figs. 10, 11, and 12). Also noted is the slight increase in cutting force when the edge radius is increased. These observations are in agreement with the observations of similar finite element models [30, 32–33]. The change in the ratio of cutting and thrust forces has been confirmed by Kang et al. [27] showing that during the micro-machining process, force components accounting for plowing and sliding increase with the decrease in uncut chip thickness, which leads to a change in the ratio of force distribution. When the radius of the edge of the tool approaches the size of the uncut chip thickness in micro-milling process, the thrust force (F_T) becomes higher in magnitude than the cutting force (F_C). Consequently, a change in the ratio of thrust-to-cutting force occurs because a transition from cutting to plowing occurs [27].

The mechanism of chip formation and chip morphology has been investigated by a number of authors who compared the simulated results with the experimentally obtained chips in order to understand chip formation micro-machining various materials. A finite element analysis has been presented for both conventional and high speed machining of Ti6Al4V alloys incorporating the Johnson-Cook and the power law models [30, 34]. The researchers investigated chip formation and morphology and compared it with experimentally generated chips. The computational predictions were almost identical to experimentally generated chips. Of course, different material models produce slightly different curvatures of the chips, but the computed shapes are largely accurate when compared with the production of chips during micro-machining. The verification of applying FEA principles to chip formation and morphology is validated by prior investigations [30, 34]. In the present work, by observing Figs. 4, 5, 6, 7, 8, and 9, it is obvious that there is a change in the chip shape as the ratio of feed per tooth and tool edge radius ($f_{\mathrm{tooth}}/t_{\mathrm{r}}$) changes in magnitude. Furthermore, as the uncut chip thickness is decreased the bending moment acting on the chip root changes the direction of the cut chip. For a ratio of feed per tooth/ tool edge radius that is close to unity ($f_{\mathrm{tooth}}/t_{\mathrm{r}} \sim 1$), the bending moment acts at the chip root, moving the chip away from the tool. As the ratio of feed per tooth/tool edge radius is decreased to 0.5 ($f_{\mathrm{tooth}}/t_{\mathrm{r}} = 0.5$), the bending moment is absent and the chip moves vertically in an upward direction. As the ratio of the feed per tooth/ tool edge radius is further decreased to approximately 0.3 ($f_{\mathrm{tooth}}/t_{\mathrm{r}} \sim 0.3$), an opposing bending moment bends the chip towards the cutting tool. The same observations were made in previous investigations [26, 28–29]. Obikawa and Usui [35] have focused their research on implementing a crack growth criterion into finite element modeling to better predict discontinuous chip formation. They incorporated a fracture strain criterion and obtained results in very close agreement to the experimental findings. The influence of the chosen material model for the FEA on chip formation has been further investigated [36–43]. The choice of the model will clearly make a difference when interpreting the chip morphology results and comparing them with the experimentally obtained shapes. The chip curl radius can be observed to be different for each material model and it is argued that the power law model provides the values closest to the experimentally generated chips. The stress patterns seem to be similar in all cases while on the other hand the actual values are somewhat different depending on the material model used in the simulations. The temperature distribution is also considered to be the same or similar in all cases. However, even though most parameters behave in a similar manner for all material models, residual stresses in the workpiece material differ significantly [36].

The change in the feed per tooth/ tool edge radius ratio ($f_{\mathrm{tooth}}/t_{\mathrm{r}}$) also produces a change in the ratio of maximum cutting/thrust forces (F_C/F_T). As the chip thickness is decreased in the ‘down-cut milling’ process, the cutting/thrust force ratio changes, and is presented in Figs. 9, 10, 11, and 12. The transition from $F_C/F_T < 1$ (burr formation) to $F_C/F_T > 1$ (chip formation) defines a transition from burr-to-chip formation and is further characterized in Tables 3, 4, 5, 6, 7, and 8 using rations, F_C/F_T and $f_{\mathrm{tooth}}/t_{\mathrm{r}}$, for the simulations presented in this study. In practice, a recent paper by Aslantas [44] has shown that nanocrystalline-coated micro-tools do not improve tool life significantly, but do minimize or eliminate the generation of burrs. However, tool life was improved using AlCrN-coated micro-tools.

For all the simulations presented, the shear strain varies between 3.5 and 4 and the position of maximum shear strain moves from the chip to the surface of the workpiece as the tool edge radius decreases in magnitude. In terms of surface quality, it is advised that the feed per tooth should be a large as possible to minimize distortion of the surface of the workpiece by inducing shear strains into the chip rather than the surface of the machined workpiece.

4.2 Spindle speed and feed effects

It has been noticed that as the value for the rotational speed increases, the thrust force values show a direct dependence on rotational spindle speed yielding higher values [24]. The rise in the thrust force with the increase in rotational speed is attributed to the adherence of the chip to the cutting tool [29]. With the increase in temperature, adherence of the chip to the tool is actively promoted. The degree of adherence is considered to increase with the increase in speed due to the increase in temperature, eventually resulting in the increase in thrust force. However, Robinson [30] showed that temperatures in micro-machining commonly used engineering materials are very low, and when micro-machining Ti6Al4V titanium alloy products, the maximum machining temperature stabilizes between 25 and 68 °C (using cemented carbide tools (uncoated)) depending upon the machining parameters. Therefore, an absence of sustained heat flow at high temperatures allows one to predict that the chips generated during micro-machining do not actually adhere to the cutting tool, and consequently thrust forces do not change with an increase in the rotational speed of the cutting tool. The stability in computed magnitudes of forces with the consequent change in the rotational speed is shown in Figs. 13 and 14. For the VFCVD diamond-coated tools, the forces are relatively stable at the three magnitudes of cutting feeds. For diamond tools, the cutting forces are relatively stable, while the thrust force shows some level of stability that could be attributed to difference in hardness between using tungsten carbide and diamond as the tool material. This observation was also noted when micro-milling AISI 1020 and 4140 steels [30] who validated the use of using FEA for analyzing forces and effects on chip formation and shape.

The influence of the feed per tooth when micro-machining Ti6Al4V titanium alloy is significant in terms cutting and thrust forces. The point at which the forces are equal is used to define the stability of the process and the recommended parameters in terms of feed per tooth, tool diameter and spindle speed. It is shown in Figs. 15 and 16 that cutting and thrust forces increase with increases in the feed/tooth. The transition points define three stages of machining: (A) burr formation, (B) mixed mode region of cutting, plowing and sliding, and (C) chip formation. There is a strong similarity when the results are compared with the results demonstrated by Kim and Kim [31] who had based their research on the differentiation of micro- and macro-cutting processes. Their research shows that the increasing force with the depth of cut is accounted for by three components of factors: the rake face, the contact point of the workpiece and the tool's clearance face, which can cause elastic spring back of the workpiece material and tool, and the rounding effect of the edge of the tool. The studies conducted in this paper appear to validate their work and that of Robinson's [30, 31].

4.3 Temperatures, distribution, and changes in heating rate

Temperature is considered to be another one of the commonly investigated issues using FEA in the process of machining. Usui et al. [37] investigated the tool edge temperature and its effect on the wear characteristics in machining with ceramic tools. The influence of the cutting speed on the temperature generated in the tool has been investigated showing that there is a significant increase in the tool temperature with a higher value registered for the rake compared with flank face of the tool [38]. The fact that the tool temperature increases with the increase in cutting speed was confirmed [37] and it has been shown that the temperatures are close to the melting temperature of the workpiece material. Kim et al. used finite element modeling to determine temperature and stress distributions in micro-machining [39]. The researchers chose oxygen free copper as the workpiece material while the tool was a diamond cutter. It was presented that the highest temperature occurred within the shear plane at it reaches 562 °C even though the depth of cut is only 2 μm. They determined that if the effect of the temperature is ignored the values obtained for the flow stress are doubled when compared with the experimental one resulting in forces considerably higher than those measured. Cao et al. [40] concluded in their research findings that the maximum cutting temperature depends greatly on the tool edge radius, and it increases with the increase in tool edge radius. It has also been noticed that the effect of the radius in not only on the magnitude of the temperature generated during machining, but on the temperature field distribution and direction as well. For VFCVD diamond-coated cutting tools, it was noted that the temperatures generated at the tool-workpiece contact zone at the micro-scale were computed to range from ~24.5 to 42 °C.

In the present work, when the change in heating rate at the point where $F_C = F_T$ is analyzed (mixed mode cutting/sliding), there is a transition of forces from $F_C/F_T < 1$ to $F_C/F_T > 1$. When $F_C/F_T < 1$, burr formation is predominant and when $F_C/F_T > 1$, the chip formation is prevalent. It can be seen from Figs. 17, 18, 19, 20, 21, 22, 23, 24, 25, 26, 27, and 28 that there is a difference in the shape and position of the thermal field. The heating rate field changes direction when there is a change from burr formation to chip formation. Before the transition, i.e., when stable machining and chip formation is present, the heating rate field is located in the chip root showing that the heat will dissipate into the chip rather than into the workpiece. The heat is then taken away by the chips from the tool and workpiece. It can be seen that the highest heating rate occurs at the chip root and is concentrated in one area with no distinctive dissipation path identified. When crossing into the region of burr formation, the heating rate field can be seen to move away from the free surface of the chip towards the tool and under the tool into the workpiece. Rather than going into the burr the heat is partitioned into the workpiece. The partitioned heat could be considered responsible for the rewelding of the cracks in the burrs as it is pushed out of the tool-work material contact zone. It can be seen that the highest heating rate is covers a larger area below the tool as well as below the chip root into the bulk of the work material. This change in the position of the heat rate field is expected to occur and is in accordance with the phenomena associated with the burr-to-chip transition [30]. The phenomenon appears to be in accordance with Cao [40] and other researchers [41–43]. In terms of surface quality, it is advised that the chip formation is promoted in order to partition the heat into the chip rather than into the workpiece material. For chip formation conditions to occur, the ration F_C/F_T should be greater than unity ($F_C/F_T > 1$) and the ration of feed per tooth to tool edge radius should be approximately unity, i.e. $f_{\mathrm{tooth}}/t_r \sim 1$ [43].

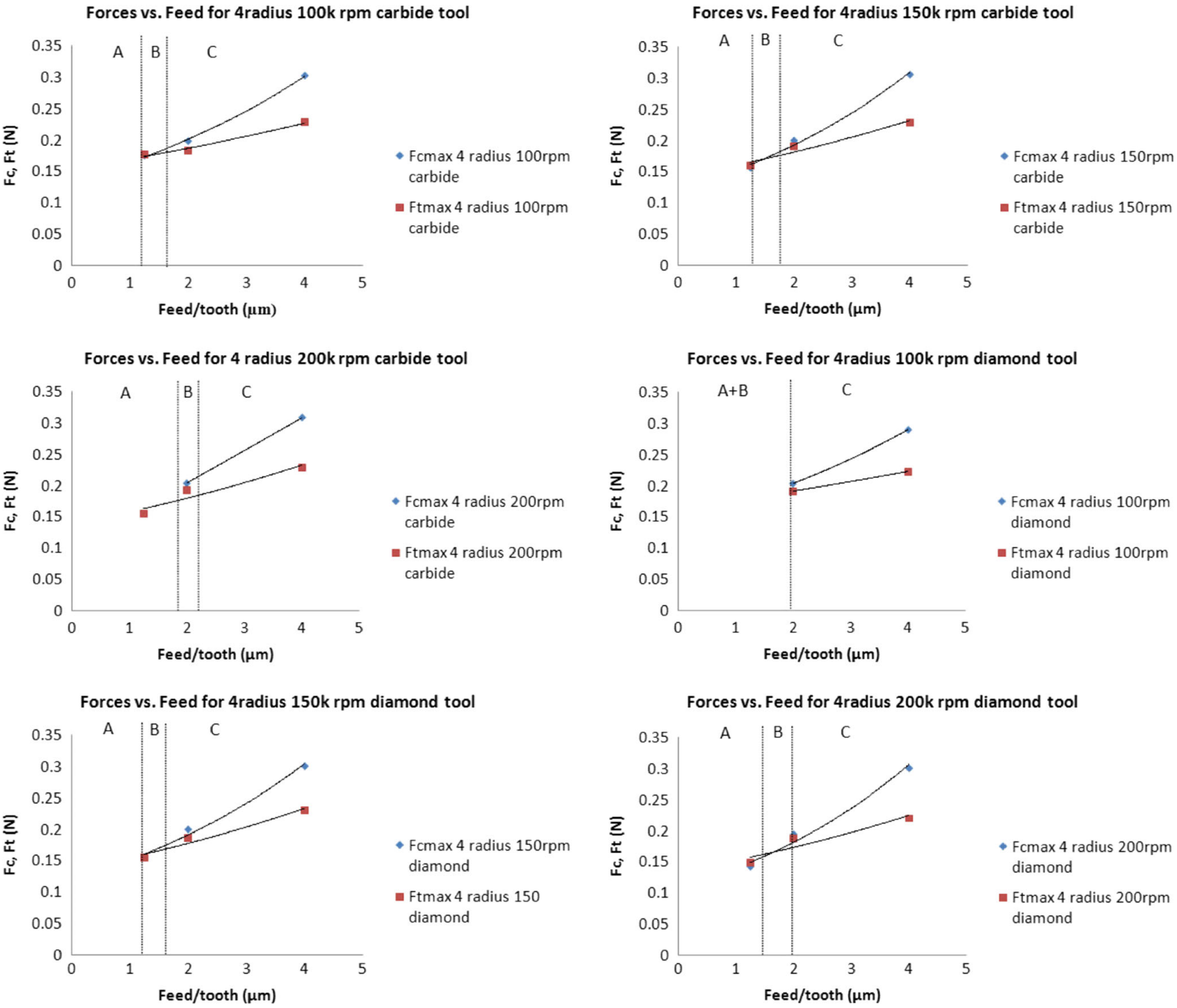

Fig. 16 Force versus feed/tooth for a 4-μm tool edge radius cutting tool at various spindle speeds and cutting tool material. **a** $F_C/F_T < 1$ (burr formation), **b** $F_C/F_T = 1$, and **c** $F_C/F_T > 1$ (chip formation)

5 Conclusions

It has been determined that when micro-machining Ti6Al4V titanium, that when the magnitude of the cutting force is higher than the thrust force ($F_C/F_T > 1$), chip formation occurs and that chip curl is caused by the bending moment which acts at the root of the chip. When the cutting and thrust forces are equal in magnitude ($F_C = F_T$), the bending moment diminishes, leaving a vertical chip to form where burr and chip formation exists simultaneously. When the cutting force is lower in magnitude than the thrust force ($F_C/F_T < 1$), chip formation ceases and burr formation is promoted. Work material detached by the cutting edge is bent towards the tool, showing an opposite bending moment when compared with the case of chip formation. Furthermore, the heating rate is seen to change drastically when the aforementioned transition occurs. During the chip formation process, the heating rate field is situated close to the root of the chip moving directly into the chip and away from the workpiece surface. As the transition to burr formation occurs, the heating rate field moves into direction of the workpiece and under the tool as the chip-to-burr transition takes place.

The transition from the chip-to-burr formation can also be observed when the ratio of feed per tooth to tool edge radius is analyzed. When the ratio of feed per tooth to tool edge radius is approximately unity ($f_{\text{tooth}}/t_r \sim 1$), the process forms chips. When the ratio is decreased to equal 0.5 ($f_{\text{tooth}}/t_r = 0.5$), chip formation and burr formation exists simultaneously. However, when the ratio approaches an approximate value of 0.3 ($f_{\text{tooth}}/t_r \sim 0.3$), burr formation is dominant. This information is considered extremely important when determining the minimum size of the features produced by the micro-milling process. Also,

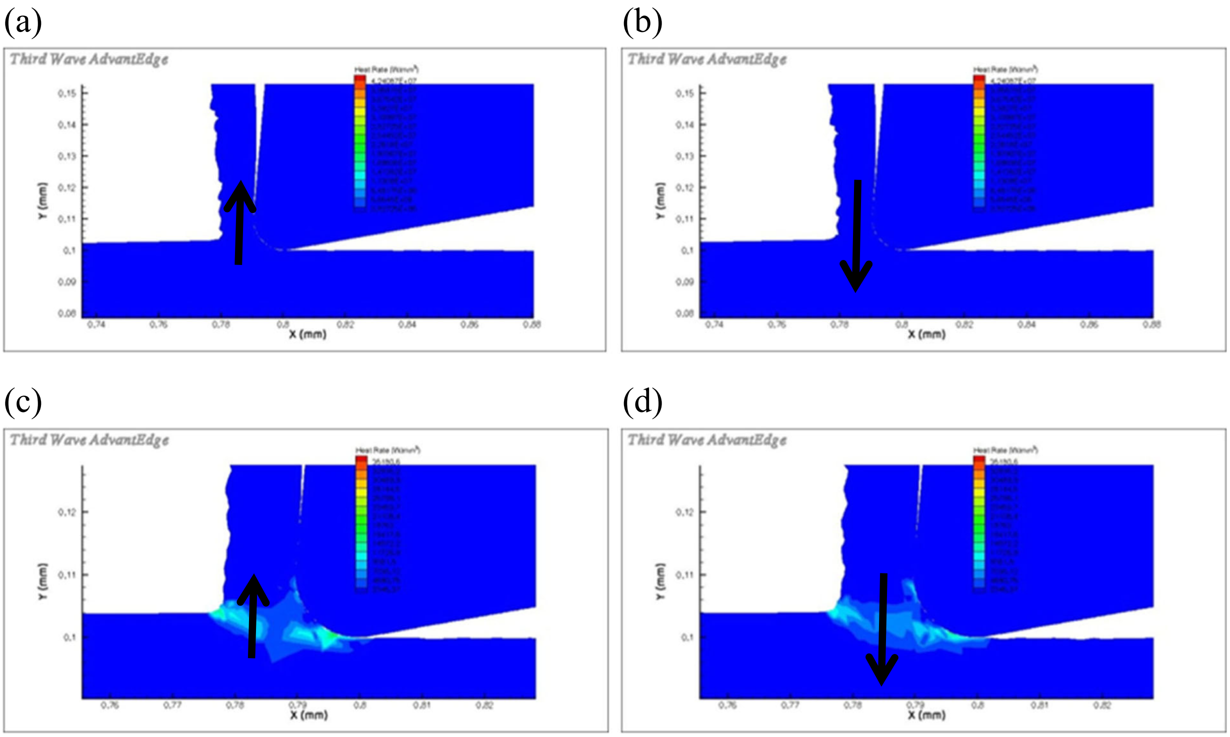

Fig. 17 The change in the direction of the heating rate for a 10-µm radius cutting tool operating at 100,000 rpm with a VFCVD diamond-coated tool: **a** 10 µm feed/tooth when $F_C/F_T > 1$ (chip formation), **b** 10 µm feed/tooth when $F_C/F_T < 1$ (burr formation), **c** 5 µm feed/tooth when $F_C/F_T > 1$ (chip formation), and **d** 5 µm feed/tooth when $F_C/F_T < 1$ (burr formation). The *arrows* show the direction of movement of the thermal field

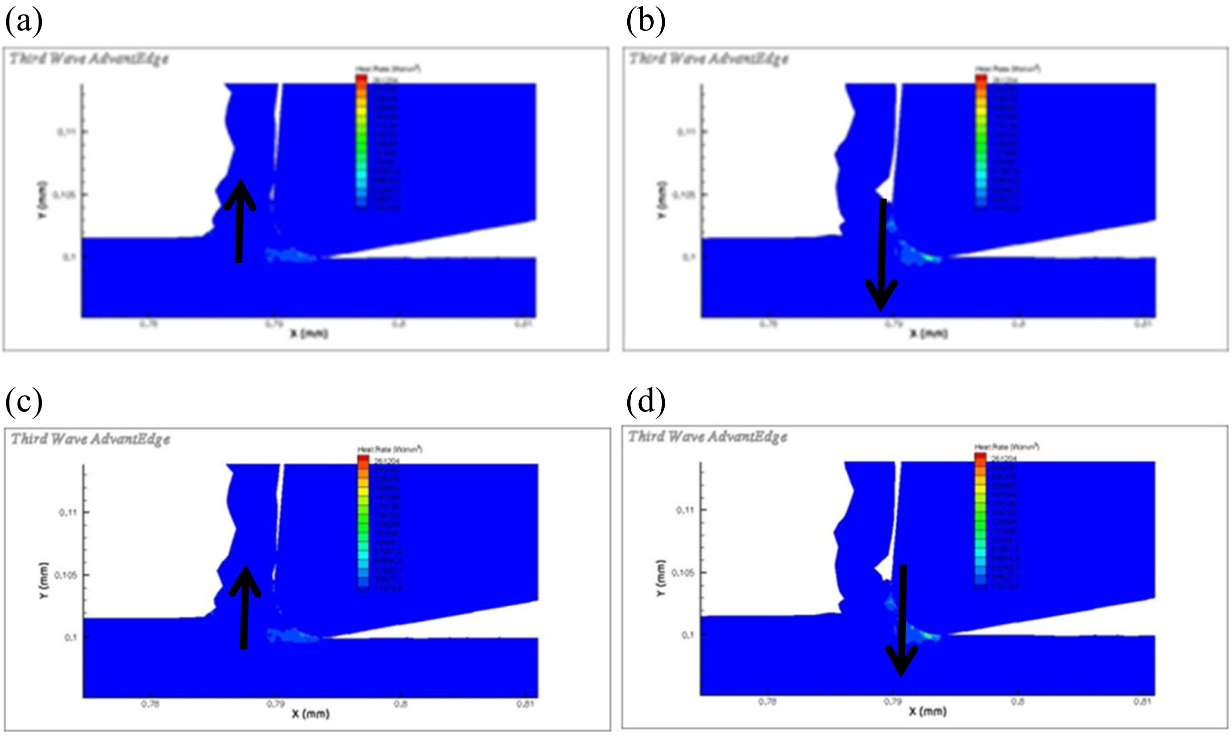

Fig. 18 The change in the direction of the heating rate for a 4-µm radius cutting tool operating at 100,000 rpm with a VFCVD diamond-coated tool: **a** 4 µm feed/tooth when $F_C/F_T > 1$ (chip formation), **b** 4 µm feed/tooth when $F_C/F_T < 1$ (burr formation), **c** 2 µm feed/tooth when $F_C/F_T > 1$ (chip formation), and **d** 2 µm feed/tooth when $F_C/F_T < 1$ (burr formation). The *arrows* show the direction of movement of the thermal field

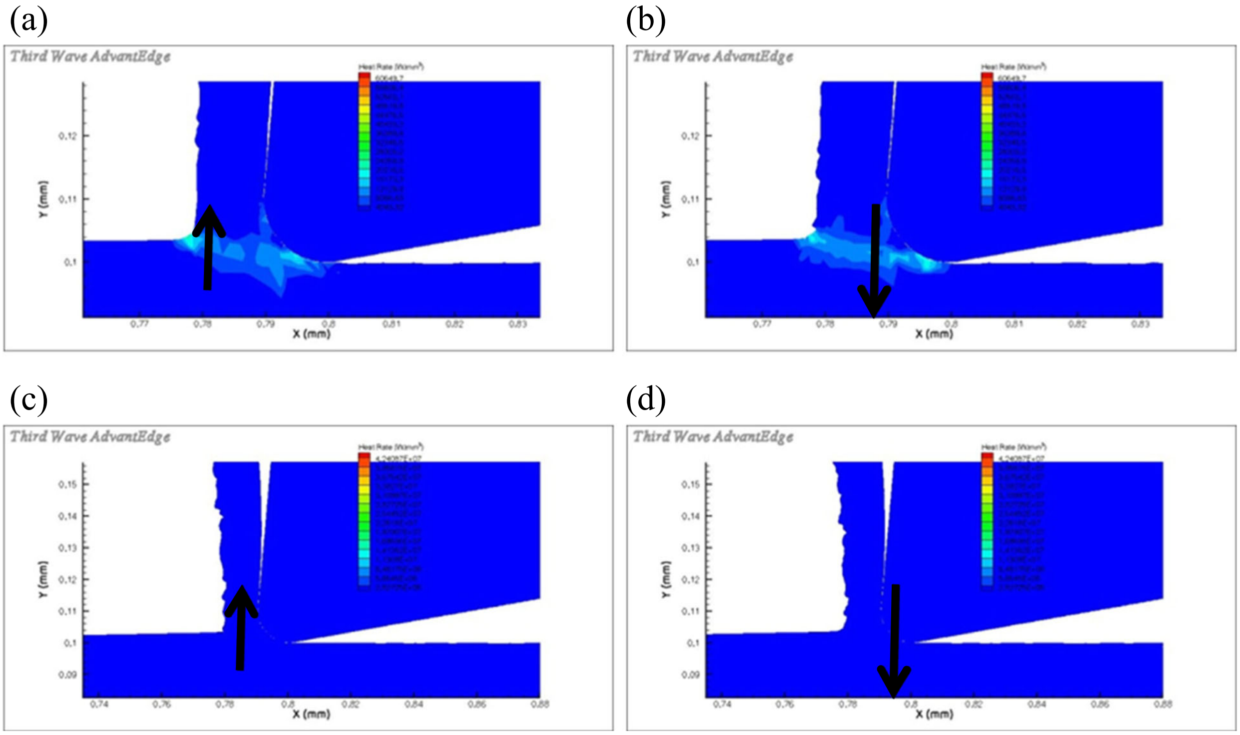

Fig. 19 The change in the direction of the heating rate for a 10-μm radius cutting tool operating at 150,000 rpm with a VFCVD diamond-coated tool: **a** 10 μm feed/tooth when $F_C/F_T > 1$ (chip formation), **b** 10 μm feed/tooth when $F_C/F_T < 1$ (burr formation), **c** 5 μm feed/tooth when $F_C/F_T > 1$ (chip formation), and **d** 5 μm feed/tooth when $F_C/F_T < 1$ (burr formation). The *arrows* show the direction of movement of the thermal field

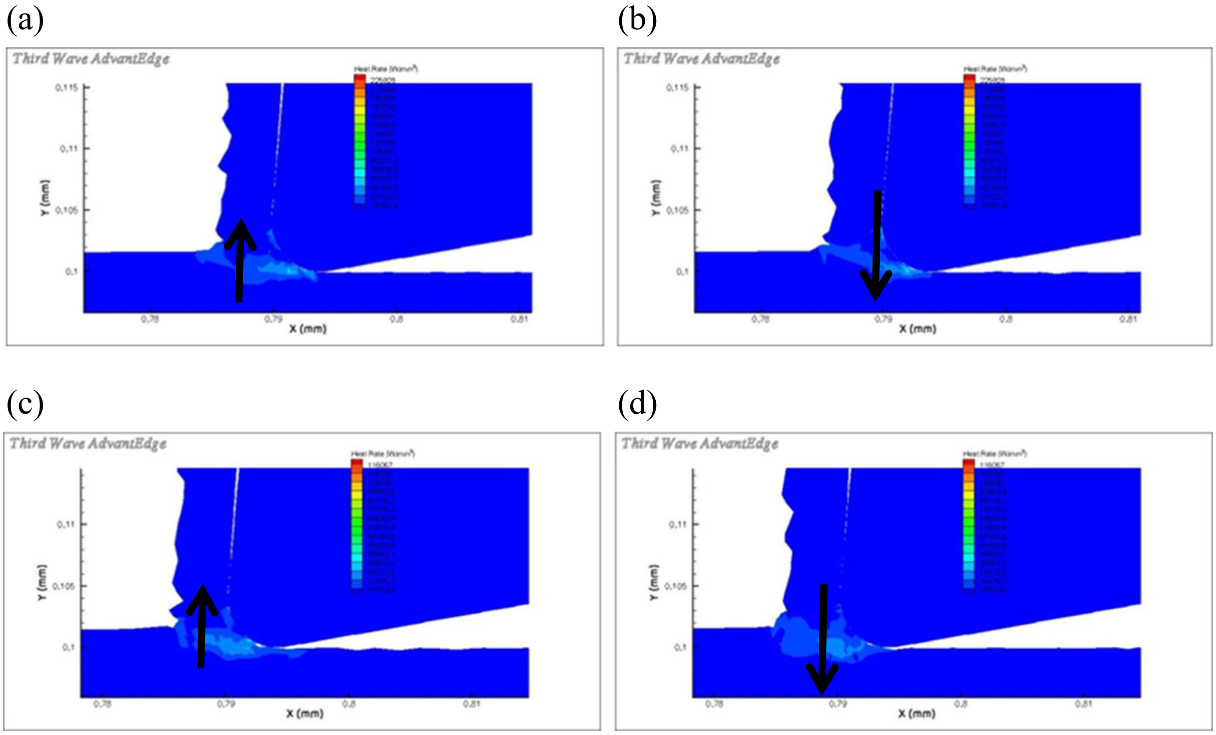

Fig. 20 The change in the direction of the heating rate for a 4-μm radius cutting tool operating at 150,000 rpm with a VFCVD diamond-coated tool: **a** 4 μm feed/tooth when $F_C/F_T > 1$ (chip formation), **b** 4 μm feed/tooth when $F_C/F_T < 1$ (burr formation), **c** 2 μm feed/tooth when $F_C/F_T > 1$ (chip formation), and **d** 2 μm feed/tooth when $F_C/F_T < 1$ (burr formation). The *arrows* show the direction of movement of the thermal field

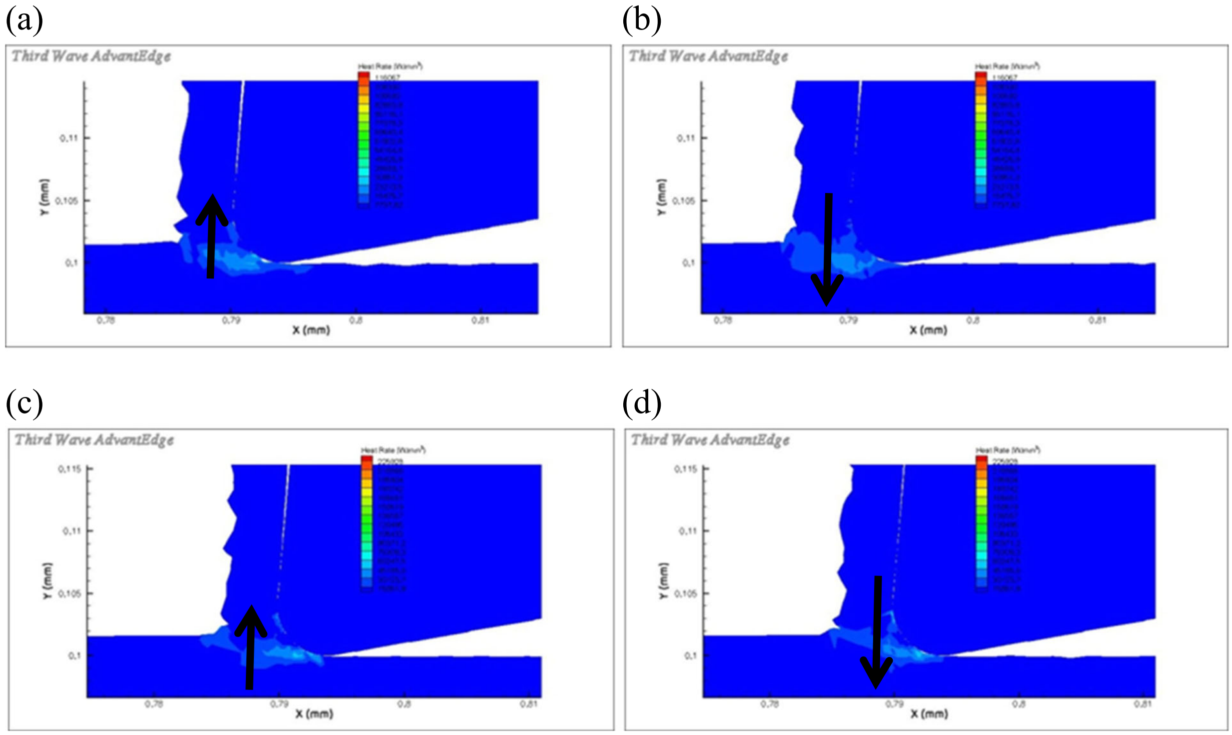

Fig. 21 The change in the direction of the heating rate for a 10-μm radius cutting tool operating at 200,000 rpm with a VFCVD diamond-coated tool: **a** 10 μm feed/tooth when $F_C/F_T > 1$ (chip formation), **b** 10 μm feed/tooth when $F_C/F_T < 1$ (burr formation), **c** 5 μm feed/tooth when $F_C/F_T > 1$ (chip formation), and **d** 5 μm feed/tooth when $F_C/F_T < 1$ (burr formation). The *arrows* show the direction of movement of the thermal field

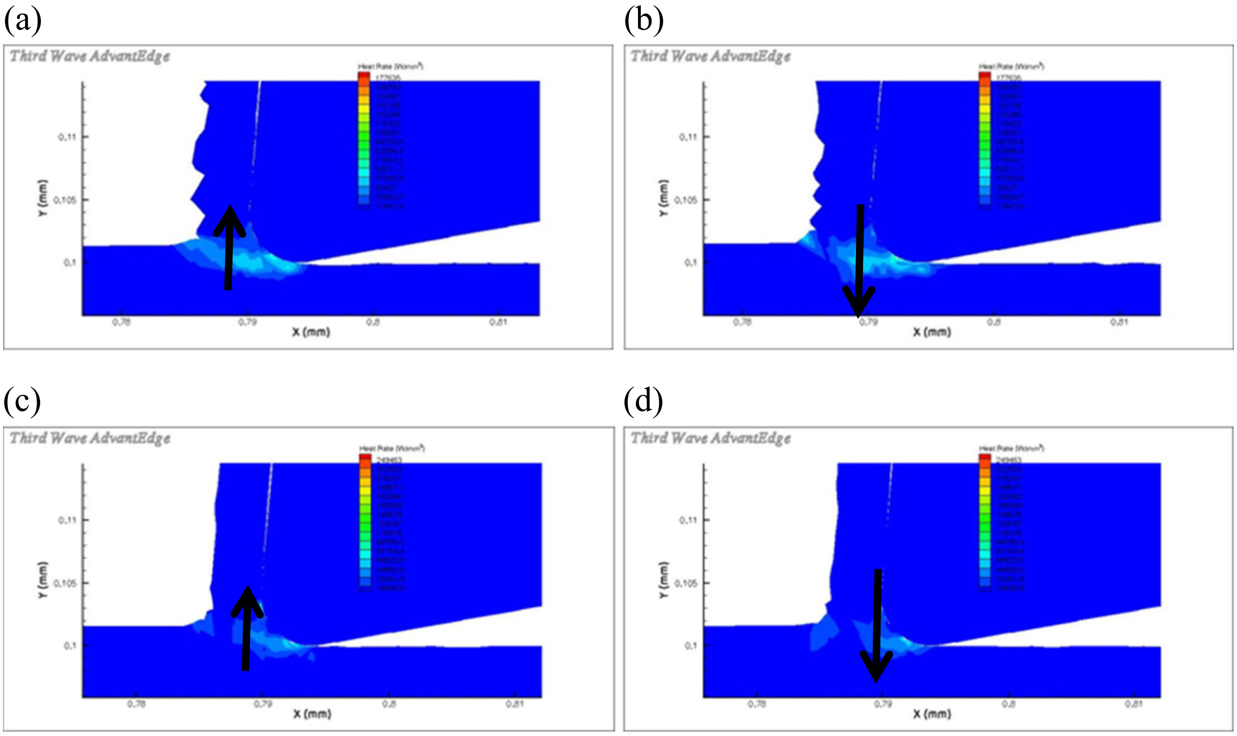

Fig. 22 The change in the direction of the heating rate for a 4-μm radius cutting tool operating at 200,000 rpm with a VFCVD diamond-coated tool: **a** 4 μm feed/tooth when $F_C/F_T > 1$ (chip formation), **b** 4 μm feed/tooth when $F_C/F_T < 1$ (burr formation), **c** 2 μm feed/tooth when $F_C/F_T > 1$ (chip formation), and **d** 2 μm feed/tooth when $F_C/F_T < 1$ (burr formation). The *arrows* show the direction of movement of the thermal field

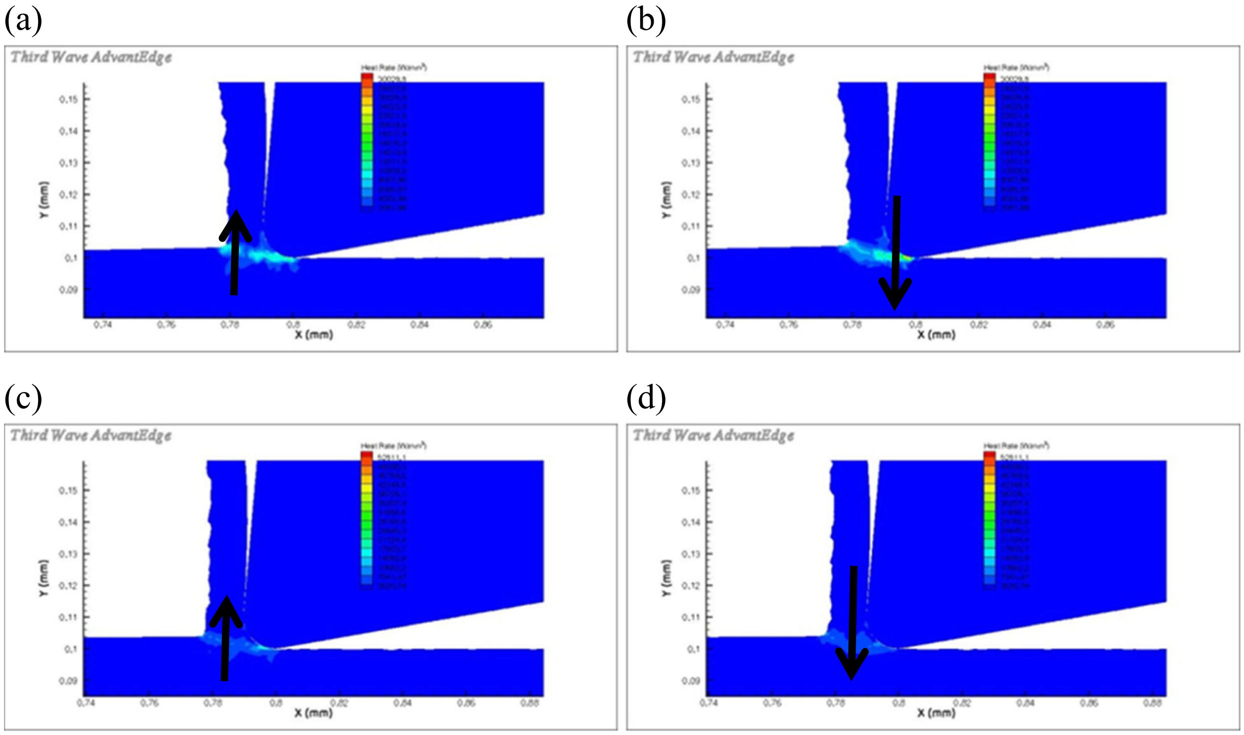

Fig. 23 The change in the direction of the heating rate for a 10-µm radius cutting tool operating at 100,000 rpm with a VFCVD diamond cutting tool: **a** 10 µm feed/tooth when $F_C/F_T > 1$ (chip formation), **b** 10 µm feed/tooth when $F_C/F_T < 1$ (burr formation), **c** 5 µm feed/tooth when $F_C/F_T > 1$ (chip formation), and **d** 5 µm feed/tooth when $F_C/F_T < 1$ (burr formation)

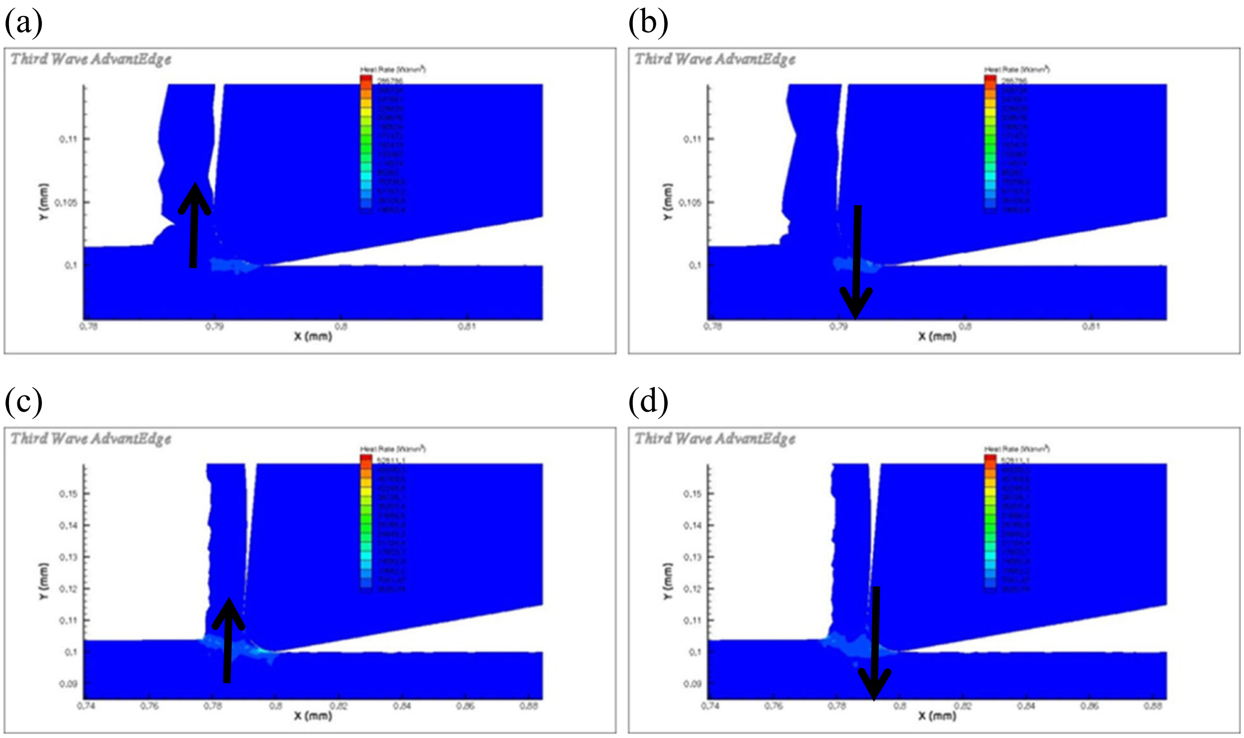

Fig. 24 The change in the direction of the heating rate for a 4-µm radius cutting tool operating at 100,000 rpm with a VFCVD diamond cutting tool: **a** 4 µm feed/tooth when $F_C/F_T > 1$ (chip formation), **b** 4 µm feed/tooth when $F_C/F_T < 1$ (burr formation), **c** 2 µm feed/tooth when $F_C/F_T > 1$ (chip formation), and **d** 2 µm feed/tooth when $F_C/F_T < 1$ (burr formation). The *arrows* show the direction of movement of the thermal field

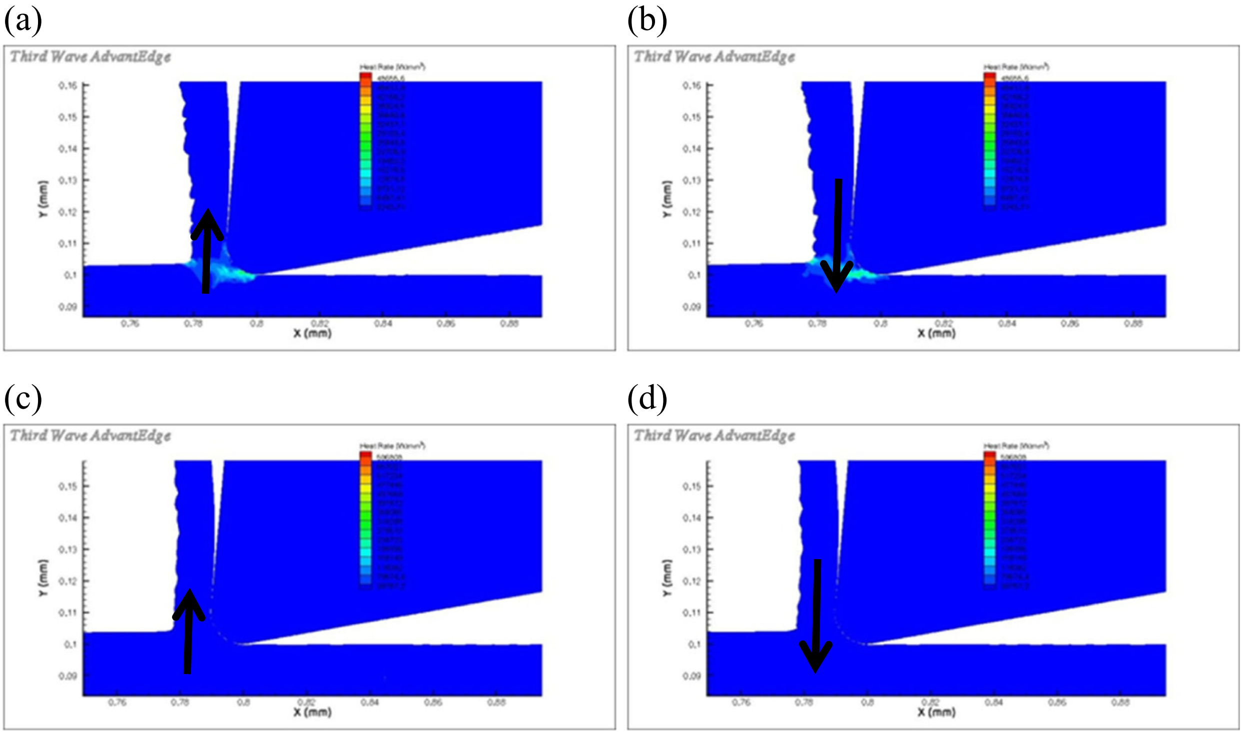

Fig. 25 The change in the direction of the heating rate for a 10-μm radius cutting tool operating at 150,000 rpm with a VFCVD diamond cutting tool: **a** 10 μm feed/tooth when $F_C/F_T > 1$ (chip formation), **b** 10 μm feed/tooth when $F_C/F_T < 1$ (burr formation), **c** 5 μm feed/tooth when $F_C/F_T > 1$ (chip formation), and **d** 5 μm feed/tooth when $F_C/F_T < 1$ (burr formation). The *arrows* show the direction of movement of the thermal field

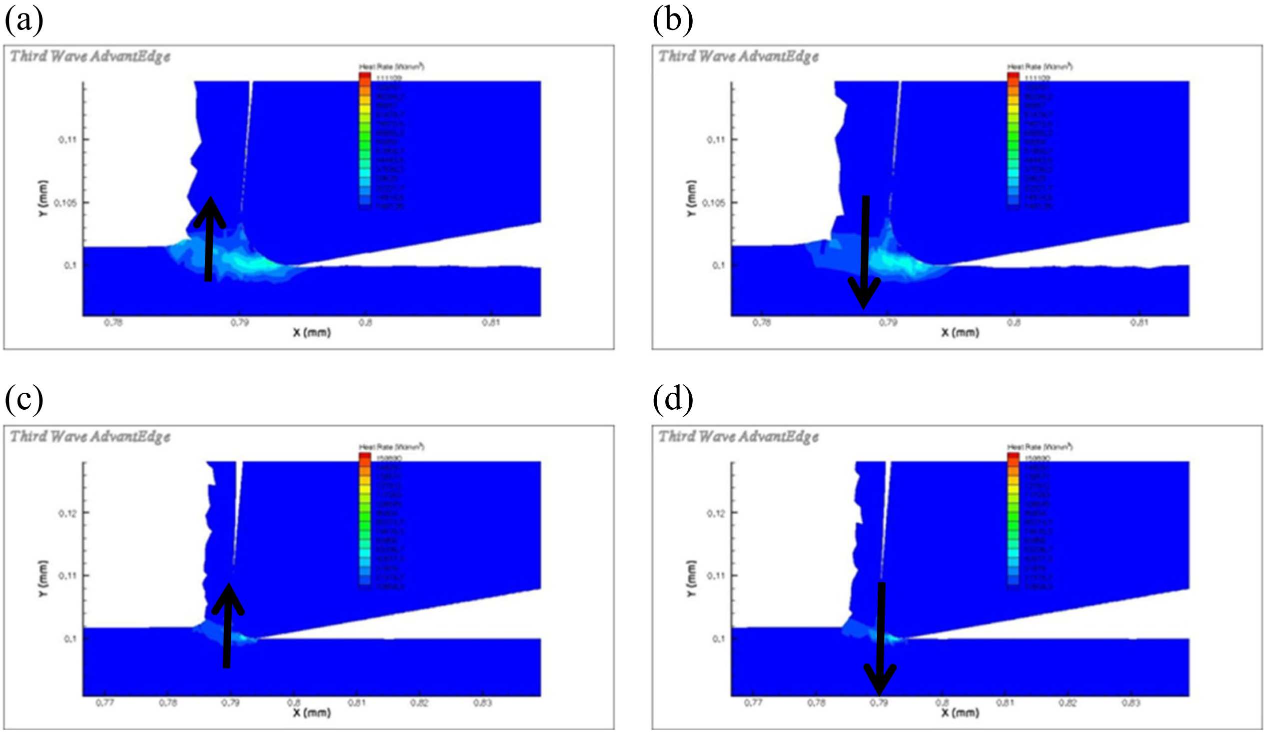

Fig. 26 The change in the direction of the heating rate for a 4-μm radius cutting tool operating at 150,000 rpm with a VFCVD diamond cutting tool: **a** 4 μm feed/tooth when $F_C/F_T > 1$ (chip formation), **b** 4 μm feed/tooth when $F_C/F_T < 1$ (burr formation), **c** 2 μm feed/tooth when $F_C/F_T > 1$ (chip formation), and **d** 2 μm feed/tooth when $F_C/F_T < 1$ (burr formation). The *arrows* show the direction of movement of the thermal field

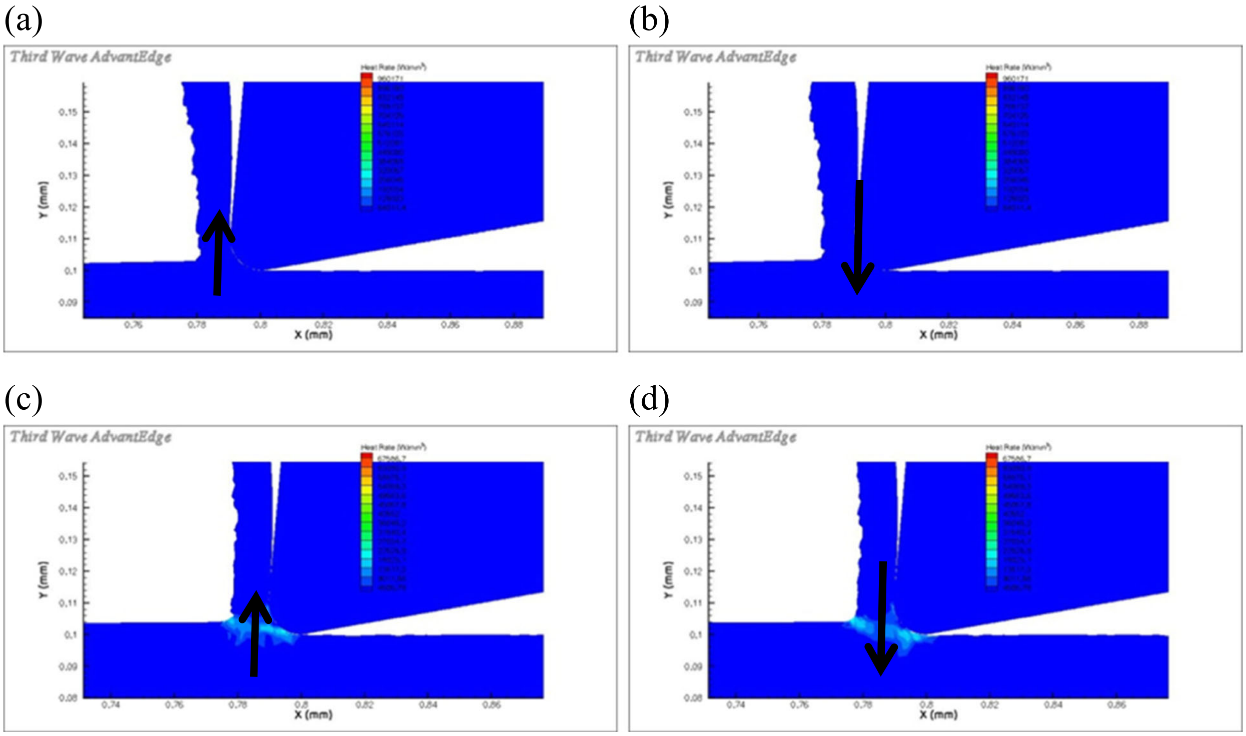

Fig. 27 The change in the direction of the heating rate for a 10-μm radius cutting tool operating at 200,000 rpm with a VFCVD diamond cutting tool: **a** 10 μm feed/tooth when F_C/F_T >1 (chip formation), **b** 10 μm feed/tooth when F_C/F_T <1 (burr formation), **c** 5 μm feed/tooth when F_C/F_T >1 (chip formation), and **d** 5 μm feed/tooth when F_C/F_T <1 (burr formation). The *arrows* show the direction of movement of the thermal field

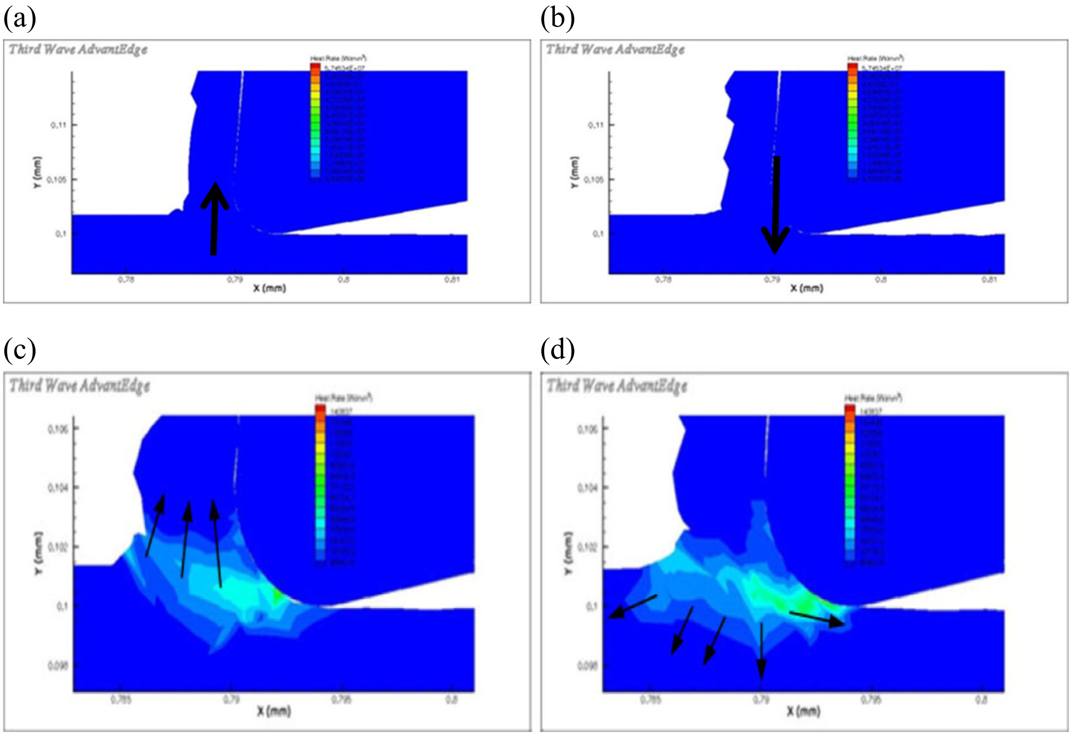

Fig. 28 The change in the direction of the heating rate for a 4-μm radius cutting tool operating at 200,000 rpm with a VFCVD diamond-coated cutting tool: **a** 4 μm feed/tooth when F_C/F_T >1 (chip formation), **b** 4 μm feed/tooth when F_C/F_T <1 (burr formation), **c** 2 μm feed/tooth when F_C/F_T >1 (chip formation), and **d** 2 μm feed/tooth when F_C/F_T <1 (burr formation). The *arrows* show the direction of movement of the thermal field

as the tool edge radius decreases in magnitude, the position of maximum shear strain moves from the chip to the surface of the workpiece material. The study has shown which parameters cause the formation of burrs when the relevant rations are incorrectly chosen.

Finally it has been determined that the rotational speed has a different influence at the micro-scale than it does at the macro-scale. Chip formation is defined by the adherence of the chip to the cutting tool due to the high temperatures generated in the macro-machining of the Ti6Al4V titanium alloy (thermal effects are clearly very important at the macro-scale). The lack of chip adherence and low temperatures generated at the tool-workpiece contact zone at the micro-scale (~24.5 to 42 °C for VFCVD diamond-coated tools) implies that a different mechanism of chip formation is operating at the micro-scale and that the mechanism is clearly dependent on kinematic and kinetic effects rather than thermal effects, as observed by other research works on the FEA of micro-machining processes [30, 32–43].

Acknowledgements The authors thank Brad Raggozino, Luis Zamorano, and Troy Marusich for discussions about the use of AdvantEdge™ software for micro-machining applications and for allowing the authors to use Third Wave Systems' AdvantEdge™ software to conduct the analysis presented in this paper.

References

1. J. P. Davim and M. J. Jackson (eds) (2009) Nano and micromachining. ISTE/Wiley Press, London, UK, 212 pp
2. D. Tolfree and M. J. Jackson (eds) (2008), Commercializing micro and nanotechnology products. CRC Press-Taylor and Francis Publishers, 269 pp
3. M. J. Jackson and W. Ahmed (eds) (2014), Emerging nanotechnologies for manufacturing, 2nd edn. William Andrew (Elsevier), Oxford, UK, 551 pp
4. M. J. Jackson (2013) Micromachining with nanostructured cutting tools. Springer Briefs in Applied Sciences and Technology: Manufacturing and Surface Engineering, pp. 1–55
5. Ahmed W, Sein H, Jackson M, Rego C, Phoenix D, Elhissi A, Crean SJ, Chemical Vapour Deposition of Diamond for Dental Tools and Burs (2014) Springer briefs in materials: manufacturing and surface engineering series. Springer-Verlag Publishers, Heidelberg, p 140
6. Ullah M, Ahmed E, Hassan IU, Jackson MJ, Ahmed W (2011) Controlling properties of micro crystalline diamond films using oxygen in a hot filament chemical vapor deposition system. Journal of Manufacturing Technology Research 3(3/4):153–165
7. Jones AN, Ahmed W, Hassan IU, Rego CA, Sein H, Amar M, Jackson MJ (2003) Impact of inert gases on the structure, properties, and growth of nanocrystalline diamond. Journal of Physics: Condensed Matter—Special Issue on Characterization and Modelling of Group IV Semiconductors 15:2969–2975
8. Sein H, Ahmed W, Rego CA, Jones AN, Amar M, Jackson MJ, Polini R (2003) C.V.D. Diamond coating on tungsten carbide dental cutting tools. Journal of Physics: Condensed Matter – Special Issue on Characterization and Modelling of Group IV Semiconductors 15:2961–2967
9. M. J. Jackson, M. D. H. Gill, H. Sein, and W. Ahmed (2003) Manufacture of diamond coated cutting tools for micro machining applications. In: Proceedings of the Institution of Mechanical Engineers (London): part L—Journal of Materials **217**, 77–83
10. Sein H, Ahmed W, Jackson MJ, Woodwards R, Polini R (2004) Performance and characterization of CVD diamond coated, sintered diamond, and WC-co cutting tools for dental and micromachining applications. Thin Solid Films 447-448:455–461
11. Kim C-J, Mayor JR, Ni J (2004) A static model of chip formation in microscale milling. Transactions of the ASME-Journal of Manufacturing Science and Engineering **126**:710–718
12. Gurin, F.V. 1967 Metal cutting using diamond tools with ground cutting edges. Maschinostryenie, Moscow
13. Kragelsky IV, Dobychin MN, Kombalov VS (1982) Friction and wear—calculations and methods. Pergamon Press Inc, New York
14. L'Vov NP (1968) Determining the minimum possible chip thickness. Machines and Tooling 40:45–46
15. Basuray PK, Misra BK, Lal GK (1977) Transition from ploughing to rubbing. Wear 43:341–349
16. Vogler MP, Devor RE, Kapoor SG (2004) On the modeling and analysis of machining performance in micro-endmilling. Part I: surface generation. ASME J Manuf Sci Eng 126:685–694
17. Son SM, Lim HS, Ahn JH (2005) Effects of the friction coefficient on the minimum cutting thickness in micro cutting. International Journal of Machine Tools & Manufacture 45:529–535
18. Shimada S et al (1993) Feasibility study on ultimate accuracy in Microcutting using molecular dynamics simulation. CIRP Ann 42: 91–94
19. Yuan ZJ, Zhou M, Dong S (1996) Effect of diamond tool sharpness on minimum cutting thickness and cutting surface integrity in ultraprecision machining. J Mater Process Technol 62:327–330
20. Sun J, Guo YB (2009) Material flow stress and failure in multiscale machining titanium alloy Ti-6Al-4V. Int J Adv Manuf Technol 41: 651–659
21. www.matweb.com. 1996–2016. Available from: http://www.matweb.com/. Accessed November 2016
22. Blazynski, T.Z., ed. (1987) Materials at high strain rates. Elsevier Applied Science Publishers
23. Wu XY, Ramesh KT, Wright TW (2003) The effect of thermal softening and heat conduction on the dynamic growth of voids. Int J Solids Struct 40:4461–4478
24. Seo S, Min O, Yang H (2005) Constitutive equation for Ti-6Al-4V at high temperatures measured using the SHPB technique. International Journal of Impact Engineering 31:735–754
25. Khan AS, Suh YS, Kazmi R (2004) Quasi-static and dynamic loading responses and constitutive modeling of titanium alloys. Int J Plast 20:2233–2248
26. Henry, S.D., K.S. Dragolich, and N.D. DiMatteo (1995) Fatigue data book: light structural alloys. ASM International
27. Kang IS, Kim SK, Seo YW (2008) Cutting force model considering tool edge geometry for micro end milling process. J Mech Sci Technol 22:293–299
28. Barry J, Byrne G, Lennon D (2001) Observations on chip formation and acoustic emission in machining Ti-6Al-4V alloy. Int J Mach Tools Manuf 41:1055–1070
29. Cotterell M, Byrne G (2008) Characterization of chip formation during orthogonal cutting of titanium alloy Ti6Al4V. CIRP J Manuf Sci Technol 1(2):81–85
30. Robinson, G. M. (2007) Wear of nanostructured coated cutting tools during mixed scale machining. Ph.D. thesis, Purdue University, West Lafayette, United States of America
31. Kim JD, Kim DS (1995) Theoretical analysis of micro cutting characteristics in ultra precision machining. J Mater Process Technol 49: 387–398

32. Özel T, Zeren E (2007) Finite element analysis of the influence of edge roundness on the stress and temperature fields induced by high speed machining. Int J Adv Manuf Technol 35(3–4):255–267
33. Li R, Shih AJ (2006) Finite element modeling of 3D turning of titanium. Int J Adv Manuf Technol 29:253–261
34. Umbrello D (2008) Finite element simulation of conventional and high speed machining of Ti6Al4V alloy. J Mater Process Technol 196:79–87
35. Obikawa T, Usui E (1996) Computational machining of Ti alloy finite element modeling. Transactions of the ASME J Manuf Sci Eng 118:208–215
36. Shi J, Liu RC (2004) The influence of material models on finite element simulation machining. Transactions of the ASME J Manuf Sci Eng 126:849–857
37. Usui E, Shirakashi T, Kitagawa T (1978) Cutting temperature and crater wear of carbide tools. Transactions of the ASME Journal of Engineering for Industry 100(2):236–243
38. Kitagawa T, Kubo A, Maekawa K (1997) Temperature and wear of cutting tools in high speed machining of Inconel 718 and Ti-6Al-6V-2Sn. Wear 202(2):515–525
39. Kim KW, Lee WY, Sin HC (1999) A finite element analysis of machining with the tool edge considered. J Mater Process Technol 86:45–55
40. Cao ZY, He N, Li L (2008) A finite element analysis of micro/meso scale machining considering the cutting edge radius. Appl Mech Mater 10-12:631–636
41. Venkatesh V, Swain N, Srinivas G, Kumar P, Barshilla H (2016) Review on the machining characteristics and research prospects of conventional microscale machining operations. Mater Manuf Process:1–28.39. doi:10.1080/10426914.2016.1151045
42. T. Novakov (2010) Computational analysis of micromachining Ti6Al4V titanium alloy. Ph.D. thesis, Purdue University, West Lafayette, United States of America
43. Jackson MJ, Novakov T, da Silva MB, Machado AR (2016) Predicting chip and non-chip formation when micromachining Ti6Al4V titanium alloy. Int J Adv Manuf Technol. doi:10.1007/s001170-016-9754-2
44. Aslantas K, Hopa HE, Percin M, Ucun I, Çicek A (2016) Cutting performance of nano-crystalline diamond (NCD) coating in micro-milling of Ti6Al4V alloy. Precis Eng 45:55–66

Reproduced with permission of copyright owner. Further reproduction prohibited without permission.